frontiers | Frontiers in Bioengineering and Biotechnology

TYPE Original Research
PUBLISHED 02 December 2024
DOI 10.3389/fbioe.2024.1450694

OPEN ACCESS

EDITED BY
Paolo Tortora,
University of Milano-Bicocca, Italy

REVIEWED BY
Regina Tavano,
University of Padua, Italy
Begoña Sot Sanz,
Centro de Investigaciones Energéticas, Medioambientales y Tecnológicas, Spain
Maliha Zahid,
Mayo Clinic, United States

*CORRESPONDENCE
Juan C. Cruz,
jc.cruz@uniandes.edu.co
Valentina Quezada,
v.quezada@uniandes.edu.co

†These authors have contributed equally to this work and share first authorship

RECEIVED 18 June 2024
ACCEPTED 18 November 2024
PUBLISHED 02 December 2024

CITATION
Salgado L, Cifuentes-Delgado PC, Orozco JC, Muñoz-Camargo C, Reyes LH, Quezada V and Cruz JC (2024) Evaluating the impact of cell-penetrating motif position on the cellular uptake of magnetite nanoparticles. *Front. Bioeng. Biotechnol.* 12:1450694. doi: 10.3389/fbioe.2024.1450694

Evaluating the impact of cell-penetrating motif position on the cellular uptake of magnetite nanoparticles

Laura Salgado[1†], Paula C. Cifuentes-Delgado[1†], Juan Camilo Orozco[2], Carolina Muñoz-Camargo[1], Luis H. Reyes[3], Valentina Quezada[1*] and Juan C. Cruz[1*]

[1]Department of Biomedical Engineering, Universidad de Los Andes, Bogotá, Colombia, [2]Center for Microscopy (MicroCore), Vice Presidency for Research and Creation, Universidad de Los Andes, Bogotá, Colombia, [3]Product and Process Design Group (GDPP), Department of Chemical and Food Engineering, Universidad de Los Andes, Bogotá, Colombia

Cell-penetrating peptides (CPPs) have been employed to enhance the cellular uptake and intracellular delivery of various nanocarriers. Among them, nanoparticles (NPs) have been used as suitable vehicles for delivering different bioactive molecules in the treatment of a diverse range of diseases. Given the pivotal role of the conjugation method of CPPs, this study aims to evaluate the impact of the position of a cell-penetrating motif (LFVCR) on the biocompatibility, cellular uptake, and endosomal escape of magnetite NPs. The designed peptide's physicochemical properties suggest they are well-suited for efficient cell penetration with minimal cytotoxicity. The resulting designed nanoconjugates were characterized using Fourier transform infrared spectroscopy (FTIR), thermogravimetric analysis (TGA), dynamic light scattering (DLS), and transmission electron microscopy (TEM). The results indicate that motif position significantly impacts the cellular uptake and endosomal escape of the designed nanobioconjugates. Key findings suggest that motif exposure enhances endocytosis-mediated cell internalization and improves endosomal escape efficiency. These results were compared with nanobioconjugates displaying previously reported CPPs. The selected nanobioconjugate demonstrated superior performance in endosomal escape and comparable cell uptake to the reference nanobioconjugates. These results, along with the nanobioconjugate's physicochemical characteristics and high biocompatibility, position the nanocarrier as a suitable candidate for delivering diverse bioactive molecules.

KEYWORDS

cell-penetrating peptides, energy-dependent cellular uptake, clathrin-mediated endocytosis, magnetite nanoparticles, cell-penetrating motif

Introduction

Cell-penetrating peptides (CPPs) are renowned for their ability to penetrate cell membranes at low micromolar concentrations without causing significant membrane damage. Typically, CPPs are short, water-soluble peptides that are partially hydrophobic and/or polybasic, comprising no more than 35 amino acid residues and exhibiting a net positive charge at physiological pH (Madani et al., 2011). Since the discovery in 1988 of the first CPPs, derived from the HIV-1 encoded TAT protein, specifically TAT (48–60) (Green and Loewenstein, 1988), numerous CPPs have been

studied, including penetratin, R9, TP10, pVEC, Pep-1, LL-37, VP22, and pISL (Lundberg and Langel, 2003; El-Andaloussi et al., 2005; Järver and Langel, 2006). CPPs often contain one or more motifs—small amino acid sequence patterns—that are associated with their cell-penetrating capacity. A well-known motif is the arginine–glycine–aspartate (RGD) motif, which facilitates translocation into target cells through cell membrane integrin receptors (Hynes, 2002). CPPs have been demonstrated to deliver a wide range of bioactive molecules, including proteins, peptides, oligonucleotides, and nanocarriers, to various cell types and cellular compartments, both *in vivo* and *in vitro* (Järver and Langel, 2006; Koren and Torchilin, 2012). The two primary cellular uptake mechanisms for CPPs include non-endocytotic (energy-independent) pathways and endocytotic pathways. The choice of uptake mechanism depends on the specific characteristics of the CPP, the cargo molecule, the cell type, and the membrane lipid composition (Trabulo et al., 2010; Madani et al., 2011).

The first step of energy-independent mechanisms involves the interaction of positively charged CPPs with negatively charged components of the cell membrane, as well as with the phospholipid bilayer. Most cationic CPPs contain arginine in their sequences. This amino acid has a guanidine head group that can form hydrogen bonds with negatively charged phosphates and sulfates on the cell membrane, facilitating internalization at physiological pH (Farkhani et al., 2014). This cationic amino acid mediates the interaction of the peptide with anionic/acidic motifs on the cell membrane in a receptor-independent manner (Bolhassani, 2011; Koren and Torchilin, 2012). Mechanisms proposed for this internalization include inverted micelle formation (Derossi et al., 1996), pore formation (Matsuzaki et al., 1996), the carpet-like model (Pouny et al., 1992), and the membrane thinning model (Lee et al., 2005). These mechanisms are highly dependent on peptide concentration, sequence, and the lipid composition of the membrane in each study (Madani et al., 2011). On the other hand, energy-dependent mechanisms for CPP uptake involve interactions with extracellular heparan sulfate (Console et al., 2003) and different types of endocytosis (Fittipaldi et al., 2003; Richard et al., 2003), such as macropinocytosis, clathrin-dependent endocytosis, caveolae-dependent endocytosis, and clathrin- and caveolae-independent endocytosis. This diversity suggests that CPP membrane translocation can occur through multiple pathways simultaneously, or that different peptides utilize different uptake mechanisms depending on their cargo and biophysical properties (Fischer et al., 2002). The uptake mechanism can also be influenced by the nature of the cargo, whether the peptides form a stable complex with their cargo, whether the cargo is covalently bound to a CPP, or how the cargo is attached (Silhol et al., 2002).

Nanoparticles (NPs) have been extensively used as therapeutic agents for cancer treatment. However, related research has also explored nanoparticle-mediated therapy for infectious, autoimmune, cardiovascular, neurodegenerative, ocular, and pulmonary diseases (Yetisgin et al., 2020). In drug delivery, NPs have emerged as suitable carriers to improve the bioavailability of hydrophobic drugs, reduce drug degradation, enable sustained and triggered release, offer targeted tumor delivery, and bind or encapsulate multiple drug molecules. They also address solubility and stability issues, thereby prolonging the circulation half-life of the drug (Zhao and Stenzel, 2018; Zeng et al., 2022; Yusuf et al., 2023). CPPs have been employed to enhance the cellular uptake and intracellular delivery of NPs, resulting in a variety of promising NP-CPP vehicles (Rong et al., 2018; Spicer et al., 2018; Wei et al., 2018; Silva et al., 2019). However, the interplay between CPPs and NPs is highly complex, and the choice of the conjugation method plays a pivotal role. It can lead to highly efficient intracellular vectors or, conversely, impair peptide functionality. Covalent linkage of CPPs to NPs is the most prominent modification strategy, providing high stability and precise control over site-selectivity, key requisites for preserving the function and properties of the peptides (Gessner and Neundorf, 2020). Nonetheless, chemical interactions between the functional groups of the peptide and those of the NPs can significantly influence the formation of the secondary structure and the preservation of bioactivity. Our research indicates that CPPs can lose or diminish their cell-penetrating capacity if the motif is not adequately exposed during the immobilization process. However, this issue has not been extensively studied. We believe that understanding this effect is crucial for developing functional nanocarriers that can be effectively translated to clinical applications.

This study aims to preliminarily evaluate the effect of the cell-penetrating motif position on the final biocompatibility, cell internalization, endosomal escape, and activation of clathrin-mediated endocytosis of magnetic NPs. Three peptides were designed using the cell-penetrating motif LFVCR, previously identified by our research group (Ruiz Puentes et al., 2022). The motif was placed at the N-terminal, middle, and C-terminal positions of the final sequences. The sequences were immobilized via the peptide C-terminal on magnetite (Fe_3O_4) nanoparticles (MNPs) using a carbodiimide-based coupling strategy. MNPs are widely used in material science, biochemistry, diagnostics, magnetic drug and gene delivery, hyperthermia, magnetic resonance imaging, and theranostics due to their biocompatibility, high saturation magnetization, chemical stability, large surface area, and ease of functionalization (Petrov and Chubarov, 2022). Additionally, we have found that MNPs are suitable nanocarriers for the delivery of drugs, plasmids, siRNA, and other (bio) molecules (Cuellar et al., 2018; Perez et al., 2019; Lopez-Barbosa et al., 2020; Ramírez-Acosta et al., 2020; Cifuentes et al., 2023). Polyethylene glycol (PEG) was employed as a spacer molecule to avoid steric hindrance on the particle surface, and the peptides were attached to PEGylated MNPs. The nanobioconjugates were characterized by their size, surface charge, thermal stability, biocompatibility, cell uptake and endosomal escape capabilities. Cell uptake and endosomal escape properties were compared with those of nanobioconjugates with previously reported CPPs, including the well-studied antimicrobial and cell-penetrating peptide Buforin II (TRSSRAGLQFPVGRVHRLLRK) (Park et al., 1996; Park et al., 2000; Fleming et al., 2008; Cuellar et al., 2018; Sadeghi et al., 2022), as well as two peptides identified by our research group: MS12 (MFVFLVLLPLVS) (Henao et al., 2022) and RD10 (RTLFVCRVGD), the CPP from which the motif was originally discovered (Ruiz Puentes et al., 2022).

Materials and methods

Materials

Iron (II) chloride tetrahydrate (98%), iron (III) chloride hexahydrate (97%), acetic acid glacial (99.7%), sodium hydroxide

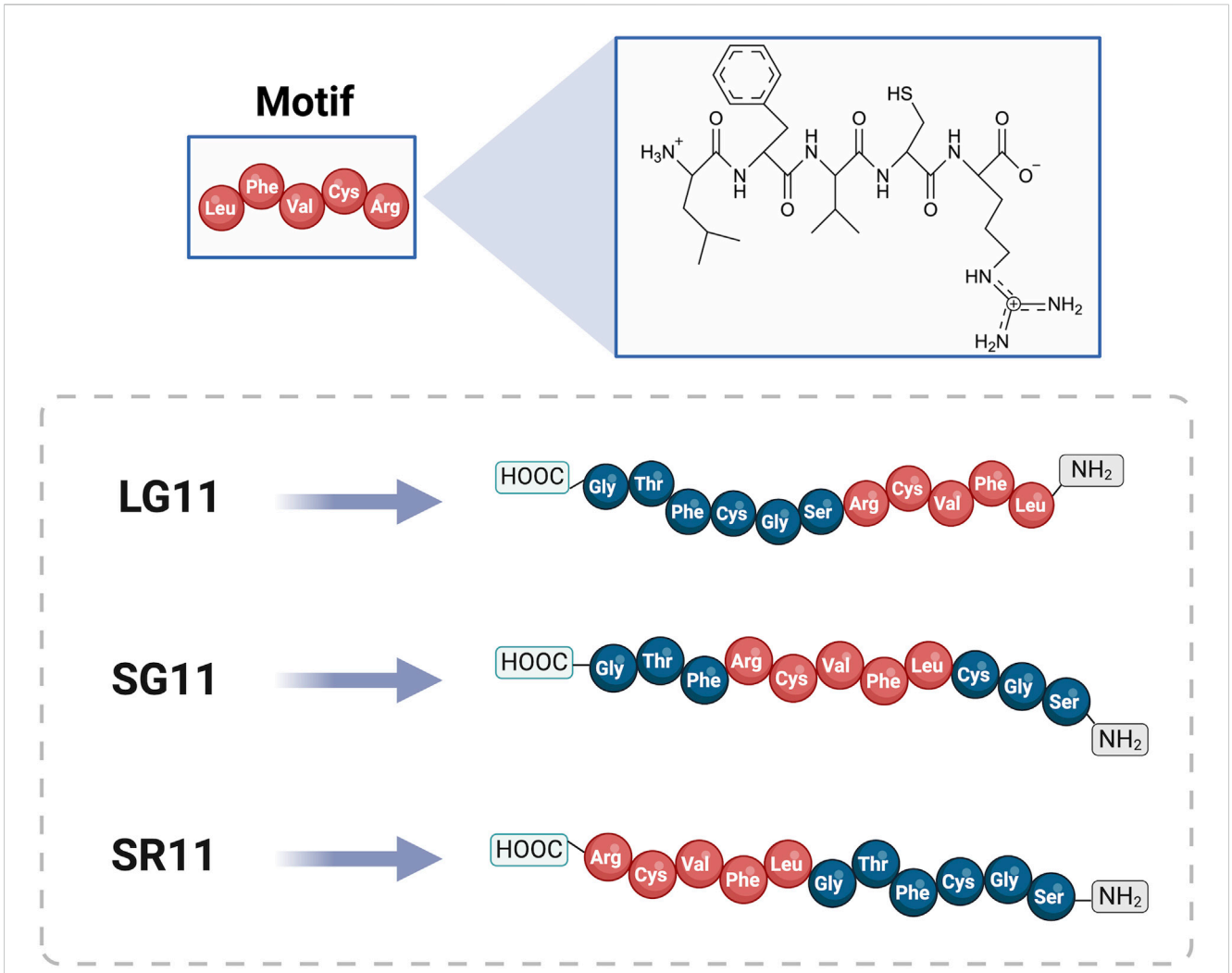

FIGURE 1
General structure of the designed peptides LG11, SG11, and SR11. The amino acids are represented by three-letter codes, with the motif sequence highlighted in red and shown with its respective chemical structure. The 3D peptide structures were generated using the I-TASSER website (https://zhanggroup.org/I-TASSER/, accessed on 5 June 2024). Created with BioRender.com.

(NaOH) (98%), and tetramethylammonium hydroxide (TMAH) (40%) were obtained from PanReac AppliChem (Barcelona, Spain). (3-aminopropyl) triethoxysilane (APTES) (98%), N-[3-(dimethylamino)-propyl]-N′-ethylcarbodiimide hydrochloride (EDC) (98%), N-hydroxysuccinimide (NHS) (98%), sodium chloride (NaCl) (99%), glutaraldehyde (25%), amine-PEG_{12}-amine (NH_2-PEG_{12}-NH_2), rhodamine B (95%), phosphate buffered saline (PBS, pH 7.2), Thrombin, Triton X-100 (laboratory grade), 3-[4,5-dimethylthiazol-2-yl]-2,5-diphenyltetrazolium bromide (MTT) and Dynasore hydrate were purchased from Sigma-Aldrich (St. Louis, MO, United States). Fetal bovine serum (FBS), and trypsin were obtained from BioWest (Riverside, MO, United States). Dulbecco's modified Eagle's medium (DMEM) was purchased from Lonza (Basel, Switzerland). 3-[(2-aminoethyl) dithiol] propionic acid (AEDP) and Hoechst 33342 were purchased from Thermo Fisher Scientific (Waltham, MA, United States). LysoTracker Green DND-26 was purchased from Novus Biologicals (Novus Biologicals, Centennial, CO, United States). Buforin II (TRSSRAGLQFPVGRVHRLLRK), MS12 (MFVFLVLLPLVS), RD10 (RTLFVCRVGD), LG11 (LFVCRSGCFTG), SG11 (SGCLFVCRFTG), and SR11 (SGCFTGLFVCR) were synthesized by GL Biochem Shanghai (Shanghai, China). Biocompatibility assays were conducted in Vero cells (ATCC®CCL-81, ATCC, St. Cloud, MN, United States).

Peptide design and physicochemical properties

The peptides were designed using the cell-penetrating motif (LFVCR), identified in a previous study via MD simulations (GROMACS version 2019.3 software). This motif was originally derived from a non-reported peptide RD10 (RTLFVCRVGD) discovered through deep learning techniques (Ruiz Puentes et al., 2022). To assess the impact of motif positioning on cell penetration efficiency, three peptides were designed with the motif located at the N-terminal, middle, and C-terminal positions within the final sequences. Graphical representations of these designed peptides and the comparative peptides (RD10, MS12, and BUFII) are provided in Figure 1 and Supplementary Figure S1, respectively.

The physicochemical parameters of the designed peptides were evaluated using different tools. Molecular weight (MW), theoretical isoelectric point (pI), and GRAVY were estimated using ProtParam, available on the bioinformatics resource portal ExPASy of the Swiss Institute of Bioinformatics website (http://web.expasy.org/protparam, accessed on 5 June 2024). Net charge at pH 7.0 was evaluated using PepCalc (https://pepcalc.com/, accessed on 5 June 2024). The Boman index was determined using APD3 (https://aps.unmc.edu/prediction, accessed on 5 June 2024). Hydrophobic moment (μH), and hydrophobicity (H) were estimated using Heliquest (https://heliquest.ipmc.cnrs.fr/cgi-bin/ComputParams.py, accessed on 5 June 2024).

Synthesis and functionalization of magnetite nanoparticles

Magnetite nanoparticles were synthesized using the chemical co-precipitation method (Cifuentes et al., 2023). Initially, 0.01 mol of $FeCl_2$ (Iron (II) chloride tetrahydrate) and 0.02 mol of $FeCl_3$ (Iron (III) chloride hexahydrate) were dissolved in 100 mL of Type I water. This solution of iron chlorides was homogenized and then cooled to 2°C. Concurrently, 0.08 mol of NaOH was dissolved in 100 mL of Type I water and cooled to 2°C.The iron chlorides solution was placed in a sealed round-bottom flask, magnetically stirred at 300 rpm, and degassed by bubbling nitrogen to remove oxygen and prevent oxidation. After 10 min, the NaOH solution was added dropwise at a rate of 5 mL/min, with constant stirring and a continuous nitrogen flow. The formation of MNPs was indicated by the appearance of a black precipitate. Following the addition of NaOH, the magnetite solution was stirred at 300 rpm for an additional hour under continuous nitrogen flow. The resultant MNPs were washed three times with a 1.5% (w/v) NaCl solution and twice with Type I water. A neodymium magnet was used to facilitate nanoparticle precipitation between washes, and sonication was applied at a frequency of 40 kHz and an amplitude of 38%.

Post-synthesis, the yield of MNPs was quantified. A 100 mg aliquot of MNPs was resuspended in 40 mL of Type I water and sonicated for 10 min at a frequency of 40 kHz and an amplitude of 38%. Subsequently, 250 μL of TMAH were added, and the solution was sonicated for 1 min under the same parameters and then magnetically stirred for 3 min. This was followed by the addition of 50 μL of glacial acetic acid, with another round of 1-min sonication and 3-min stirring. Finally, 1 mL of APTES (20% v/v) was slowly added to the MNPs solution and allowed to react at 60°C with constant stirring at 200 rpm for 1 h. The silanized nanoparticles were then washed as described previously and stored at 4°C until further use.

Synthesis of nanobioconjugates

An aliquot of 100 mg of silanized MNPs (MNPs-Si) was dispersed in 40 mL of Type I water and sonicated for 10 min at a frequency of 40 kHz with an amplitude of 38%. Following this, 2 mL of 2% (v/v) glutaraldehyde was added to the MNPs-Si suspension, which was then stirred at 250 rpm for 1 h at 24°C. Subsequently, 100 μL of NH_2-PEG_{12}-NH_2 (2 mg/mL) was added dropwise and allowed to react under mechanical agitation at 250 rpm for 24 h. The resulting PEGylated MNPs (MNPs-Si-PEG) were washed and stored as described previously.

The immobilization process aimed to conjugate the carboxyl end of the peptide to the free amine of the PEG, forming an amide bond and allowing to evaluate the motif position. Initially, an aliquot of the peptide was prepared by centrifuging the lyophilized peptide vial for 1 min at 16,000 × *g*, followed by reconstitution in 1 mL of Type I water. Concurrently, 12.3 mg of EDC and 7.4 mg of NHS were dissolved in 10 mL of Type I water. The peptide solution was then added to the EDC/NHS solution and stirred at 250 rpm for 15 min. Subsequently, the EDC/NHS-activated peptide solution was added into the PEGylated MNPs solution and allowed to react for 24 h under mechanical agitation at 250 rpm. The resulting nanobioconjugates were washed and stored as described previously. The synthesis process of the nanobioconjugates is depicted in Figure 2.

Physicochemical characterizations

The morphology of bare MNPs was examined using transmission electron microscopy (TEM) with a Tecnai F30 instrument (FEI Company, Fremont, CA, United States). The hydrodynamic diameter of the nanoparticles was determined via dynamic light scattering (DLS) analysis using a Zeta-Sizer Nano-ZS (Malvern Panalytical, Malvern, United Kingdom). To prepare for DLS, nanoparticles were diluted in Type I water to a 1% (w/v) concentration, following manufacturer guidelines, and subjected to sonication in an ultrasonic bath to prevent aggregation. Simultaneously, the zeta potential of the nanobioconjugates was measured using the same instrument at room temperature to assess surface charge. DLS and zeta potential measurements were conducted in Type I water at pH 7.4, PBS 1X, DMEM and DMEM supplemented with 10% (v/v) FBS to study aggregation in different solutions. Confirmation of stepwise immobilization on the MNPs was achieved through Fourier transform infrared spectroscopy (FTIR) using a Bruker Alpha II FTIR Eco-ATR (Bruker, Billerica, MA, United States). The absorbance spectra were collected from 4,000 cm^{-1}–600 cm^{-1} with a spectral resolution of 2 cm^{-1}, providing detailed information on chemical bonds and functional groups. The second derivative of free peptides and nanobioconjugates was calculated using OPUS spectroscopy software to assess changes in the secondary structure of the peptides following immobilization. Thermal stability and conjugation efficiency of the nanoparticles were assessed using thermogravimetric analysis (TGA) performed on a simultaneous TGA/DSC instrument (TA Instruments, New Castle, DE, United States). Each nanobioconjugate sample (approximately 2–8 mg of freeze-dried material) underwent a linear temperature ramp from 25°C to 800°C at a rate of 10°C/min under a nitrogen atmosphere flowing at 100 mL/min. The peptide immobilization efficiency was calculated using Equation 1.

$$\textit{Immobilization efficiency}\ (\%) = \left[\frac{\textit{Peptide content}}{\textit{Total amount of peptide}}\right] * 100\% \quad (1)$$

10.3389/fbioe.2024.1450694

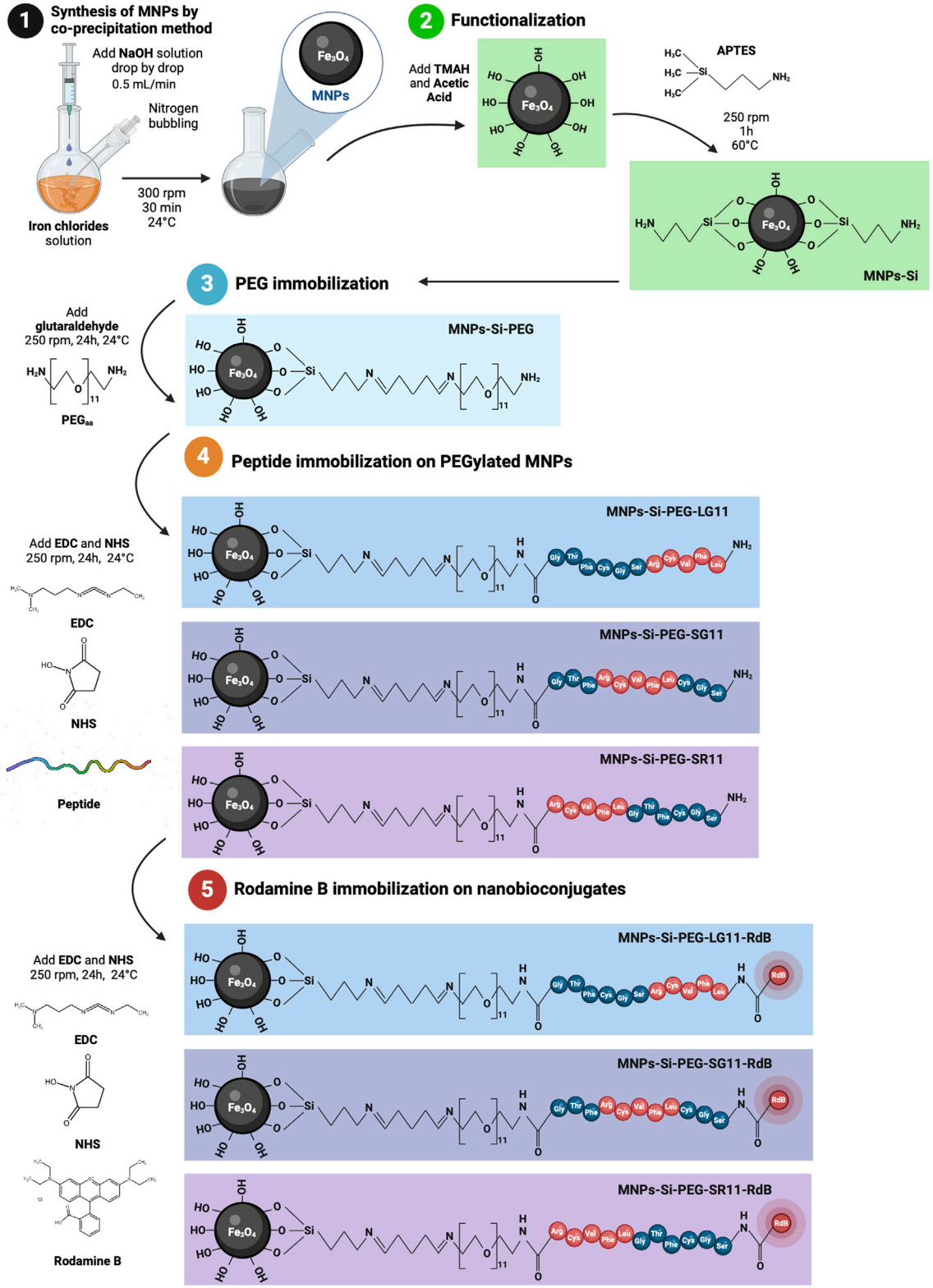

FIGURE 2
Synthesis of the nanobioconjugates. The process involves: MNP synthesis via the co-precipitation method, APTES functionalization, PEGylation of the functionalized MNPs, immobilization of the designed peptides onto the PEGylated MNPs, and Rhodamine B labeling of the peptide-based nanobioconjugates. Illustrations created with BioRender.com.

The *peptide content* was determined based on TGA results (Fadnavis et al., 2003), calculated as the difference in third-step weight loss between the nanobioconjugates and the PEGylated-MNPs. The *total amount of peptide* refers to the amount initially added during the immobilization process.

Biocompatibility studies

Hemolysis

Hemocompatibility was assessed following the ISO 10993–4: 2018 (International Organization for Standardization, 2018). Blood samples were freshly collected from a healthy human donor into a vacutainer tube containing EDTA, with permission granted by the ethics committee at Universidad de Los Andes (minute number 928–2018). Erythrocytes were isolated by centrifugation at 1800 rpm for 5 min, followed by removal of the plasma phase. Erythrocytes were washed with PBS 1X three times. To form a stock solution, 2 mL of the washed erythrocytes (4.5×10^6 erythrocytes/μL) were suspended in 18 mL of PBS 1X and carefully homogenized. The nanobioconjugates were tested at serial dilutions ranging from 100 μg/mL to 6.25 μg/mL in PBS 1X, with Triton X-100 (10% v/v) and PBS 1X serving as positive and negative controls, respectively. For hemolytic activity evaluation, 100 μL of each treatment was mixed with 100 μL of the erythrocyte stock solution in a 96-well microplate. After incubation at 37°C with 5% CO_2 for 1 h, the plate was centrifuged at 1800 rpm for 5 min. Subsequently, 100 μL of the supernatant was transferred to another 96-well microplate, and the absorbance was measured at 450 nm using a microplate reader. Hemolysis percentage was calculated according to Equation 2.

$$\textbf{\textit{Hemolysis}}\ (\%) = \left[\frac{\textbf{\textit{Abs}}(s) - \textbf{\textit{Abs}}(-)}{\textbf{\textit{Abs}}(+) - \textbf{\textit{Abs}}(-)}\right] * \textbf{100\%} \qquad (2)$$

Here, $Abs(s)$ represents the absorbance of the sample, $Abs(-)$ represents the absorbance of the negative control, and $Abs(+)$ represents the absorbance of the positive control.

Platelet aggregation assay

The platelet aggregation assay was conducted in accordance with the ISO 10993–4:2018 standard (International Organization for Standardization, 2018). Blood samples were freshly collected from a healthy human donor into a vacutainer tube containing sodium citrate, with approval from the ethics committee at Universidad de Los Andes (minute number 928–2018). The blood was centrifuged at 1,000 rpm for 20 min at room temperature to obtain Platelet-rich plasma (PRP). The supernatant containing PRP was collected for use in the assay. Nanobioconjugates were tested at serial dilutions ranging from 100 μg/mL to 6.25 μg/mL. Thrombin (9U) served as the positive control, while PBS 1X was used as the negative control, to compare the aggregation of the platelets. Platelet aggregation potential was assessed by mixing 50 μL of PRP with 50 μL of the respective treatment dilutions in a 96-well microplate. After incubating at 37°C for 5 min, absorbance was measured at 620 nm using a microplate reader. The percentage of platelet aggregation was calculated according to Equation 3.

$$\textbf{\textit{Platelet aggregation}}\ (\%) = \left[\frac{\textbf{\textit{Abs}}(s) - \textbf{\textit{Abs}}(b)}{\textbf{\textit{Abs}}(+)}\right] * \textbf{100\%} \qquad (3)$$

A standard curve was assessed, and the absorbance of the sample was normalized relative to the absorbance of the nanobioconjugates at 620 nm. Here, $Abs(s)$ represents the absorbance of the sample, $Abs(b)$ represents the absorbance of the nanobioconjugates, and $Abs(+)$ represents the absorbance of the positive control.

Cytotoxicity

The cytotoxicity of the nanobioconjugates was evaluated on Vero cells (ATCC® CCL-81) by measuring the metabolic activity associated with the conversion of MTT to formazan. The ISO 10993–5: 2009 standard was followed (ISO, 2009). The nanobioconjugates were tested across serial dilutions ranging from 100 μg/mL to 6.25 μg/mL. For the assay, 100 μL of a cell stock solution (1×10^4 cells/well) in DMEM medium supplemented with 5% (v/v) FBS was added to a 96-well microplate and incubated at 37°C with 5% CO_2 for 24 h. After the initial 24-h incubation, the supplemented DMEM medium was replaced with non-supplemented DMEM medium containing the different concentrations of nanobioconjugates. Cell viability was assessed at 24 and 48-h intervals post-incubation at 37°C, 5% CO_2. Following the same methodology described above, the cytotoxic effects of labeled and unlabeled nanobioconjugates were compared by evaluating both at a concentration of 25 μg/mL after 0.5 and 4 h of exposure. This assessment was conducted to determine any impact of the labeled nanobioconjugates on cell viability during cellular internalization and endosomal escape assays. For the MTT assay, 10 μL of MTT (5 mg/mL) was added to each well and left to react for 2 h. Then, the culture media were replaced with 100 μL of DMSO to dissolve the formazan crystals formed. Absorbance was measured at 595 nm using a microplate reader. Cell viability was calculated following Equation 4.

$$\textbf{\textit{Cell viability}}\ (\%) = \left[\frac{\textbf{\textit{Abs}}(s) - \textbf{\textit{Abs}}(t)}{\textbf{\textit{Abs}}(t) - \textbf{\textit{Abs}}(c)}\right] * \textbf{100\%} \qquad (4)$$

Here, $Abs(s)$ represents the absorbance of the sample, $Abs(t)$ represents the absorbance of the cells exposed to 1% (v/v)-Triton X-100, and $Abs(c)$ represents the absorbance of the cells that were not exposed to any treatment.

Procoagulant activity

The procoagulant activity of the nanoparticles was assessed following protocols from previous studies (Avsievich et al., 2019; Bian et al., 2019). Fresh blood samples were collected from a healthy human donor into EDTA-containing vacutainer tubes, with ethical approval from the Universidad de Los Andes (approval number 928–2018). After centrifugation at 2,500 rpm for 10 min, platelet-rich plasma and buffy coat were removed by aspiration. The erythrocytes were washed three times with PBS 1X, and 8 μL of the washed erythrocytes were added to 1 mL of nanoparticle solution (100 μg/mL) prepared in PBS 1X. Samples were incubated for 2 h at 25°C and centrifuged again under the same conditions. To prevent erythrocyte aggregation and facilitate single-cell measurements, the erythrocytes with nanobioconjugates were collected from the bottom of the tube and diluted in platelet-poor plasma (PPP) at a ratio of 1:10 μL (RBCs: PPP). Erythrocyte aggregation was

analyzed at a multicellular level by capturing light microscopy images using a Zeiss™ Primo Star Microscope (Zeiss, Germany) with a 40X/0.65 objective. Single cells and aggregates were quantified using Fiji-ImageJ® software.

To obtain PPP (Avsievich et al., 2019), fresh blood samples were collected as described above and centrifuged at 3,000 × *g* for 10 min. The supernatant was collected and centrifuged again under the same conditions, with the resulting supernatant serving as the PPP.

Labeling of nanobioconjugates with Rhodamine B

To facilitate the tracking of nanobioconjugates during confocal microscopy analyses, they were labeled with Rhodamine B. Initially, 12.3 mg of EDC and 7.4 mg of NHS were dissolved in 5 mL of Type I water. Subsequently, 5 mg of Rhodamine B was added to the solution and allowed to react under constant stirring (250 rpm) in a dark room for 15 min at 40°C to activate the carboxyl groups. This Rhodamine B solution was then added to 100 mg of each nanobioconjugate (previously resuspended in 40 mL of Type I water) and left to react for 24 h under mechanical agitation (250 rpm), covered in aluminum foil to protect from light. After labeling, the nanoparticles were washed with a 1.5% (w/v) NaCl solution until no Rhodamine B remained in the supernatant, followed by two washes with Type I water to remove excess salts, aided by a neodymium magnet. The labeled nanoparticles were stored at 4°C in complete darkness until further use.

Cellular internalization pathways and endosomal escape analysis

The cellular uptake and endosomal escape of the nanobioconjugates were investigated using confocal microscopy in Vero cells. Cells were resuspended in DMEM medium supplemented with 5% (v/v) FBS. A stock solution with a density of 150,000 cells/mL was prepared, and 100 µL was added to glass slides pre-treated with poly-D lysine. After a 24-h incubation period to allow for cell attachment, the medium was replaced with the route inhibitor. Dynasore hydrate was used to inhibit clathrin-mediated endocytosis (McCluskey et al., 2013; Preta et al., 2015). Specifically, Dynasore inhibits the GTPase activity of dynamin1, dynamin2, and Drp1, the mitochondrial dynamin. Additionally, it may interfere with cholesterol homeostasis and actin dynamics (Macia et al., 2006; Preta et al., 2015). This inhibitor was prepared at a concentration of 150 µM (Piccini et al., 2015) in non-supplemented DMEM medium.

Two sets of experiments were conducted: one with the clathrin pathway inhibitor and the other without inhibitor. For the inhibition experiment, the Dynasore solution was added to the glass slides and incubated under a humidified atmosphere at 37°C with 5% CO_2 for 30 min. Subsequently, cells were exposed to Rhodamine B-labeled nanobioconjugates in non-supplemented DMEM medium at a concentration of 25 µg/mL for 30 min and 4 h. For the test without the inhibitor, cells were exposed to the nanobioconjugate solution and evaluated under the same conditions. After exposure, cells were washed with PBS 1X and stained with Hoechst 33342 (1:10,000) and Lysotracker Green DND-26 (1:10,000) in non-supplemented medium for 5 min to label nuclei and endosomes, respectively. Following exposure, cells were washed with PBS 1X and then stained with Hoechst 33342 (1:10,000) and Lysotracker Green DND-26 (1:10,000) in non-supplemented medium for 5 min to label the nuclei and endosomes, respectively. Images were captured using an Olympus FV1000 confocal laser scanning microscope (CLSM) (Olympus, Japan) equipped with a 20X/0.75 UPlanSApo and a 40X/0.6 UCPlan FL N objetive. Excitation/emission wavelengths of 358 nm/461 nm, 488 nm/520 nm, and 546 nm/575 nm were used to detect nuclei, endosomes, and Rhodamine B-labeled nanobioconjugates, respectively. The analysis involved capturing 10 images for each treatment (10 cells per image). Image analysis was performed using Fiji-ImageJ® software to calculate colocalization and the percentage of the area covered by the nanobioconjugates.

Statistical analysis

All data measurements are presented as mean ± standard deviation from experiments conducted in triplicate. Statistical analysis was performed using GraphPad Prism 10.2.1 software (San Diego, CA, United States). Statistical comparisons were conducted using one-way or two-way ANOVA followed by Sidak's or Tukey's multiple comparisons test, as appropriate. Results were considered statistically significant at a p-value ≤ 0.05 (*), where * denotes a significant difference with a p-value in the range of $0.01 \leq p < 0.05$, ** for $0.001 \leq p < 0.01$, *** for $0.0001 \leq p < 0.001$, and **** for $p < 0.0001$.

Generative AI use

Generative AI technology, specifically OpenAI's ChatGPT (version GPT-4, model "gpt-4-turbo-16k"), was used to enhance the text by suggesting revisions for clarity and conciseness. The authors reviewed and approved all edits to ensure the content's accuracy and alignment with the research objectives.

Results and discussion

Physicochemical properties of the peptides

The physicochemical properties of the designed peptide sequences are summarized in Table 1. The designed peptides LG11, SG11 and SR11 had a net positive charge at physiological pH. Glycosaminoglycans (GAGs) and proteoglycans are critical molecules that are exposed at the outer surface of the lipid bilayer and important for CPP cell entry. Particularly, heparan sulfate and other sulfated GAGs attract cationic CPPs by their negative charges, thus acting as primary binding site for CPPs and subsequent internalization of the peptide (Neundorf, 2019). Hydrophilic peptides typically have a low or negative GRAVY score, while hydrophobic peptides have a high positive GRAVY score (Kyte and Doolittle, 1982). The positive GRAVY scores for LG11, SG11, and SR11 indicate that these peptides are hydrophobic. Hydrophobic peptides are more likely to interact with the lipid

TABLE 1 Designed peptides physicochemical properties.

Residues	MW (g/mol)	Net charge at pH 7	GRAVY	Theoretical pI	Hydrophobicity (H)	Hydrophobic moment (μH)	Boman Index
11	1,189.42	+0.91	1.073	8.07	0.799	0.182	0.13

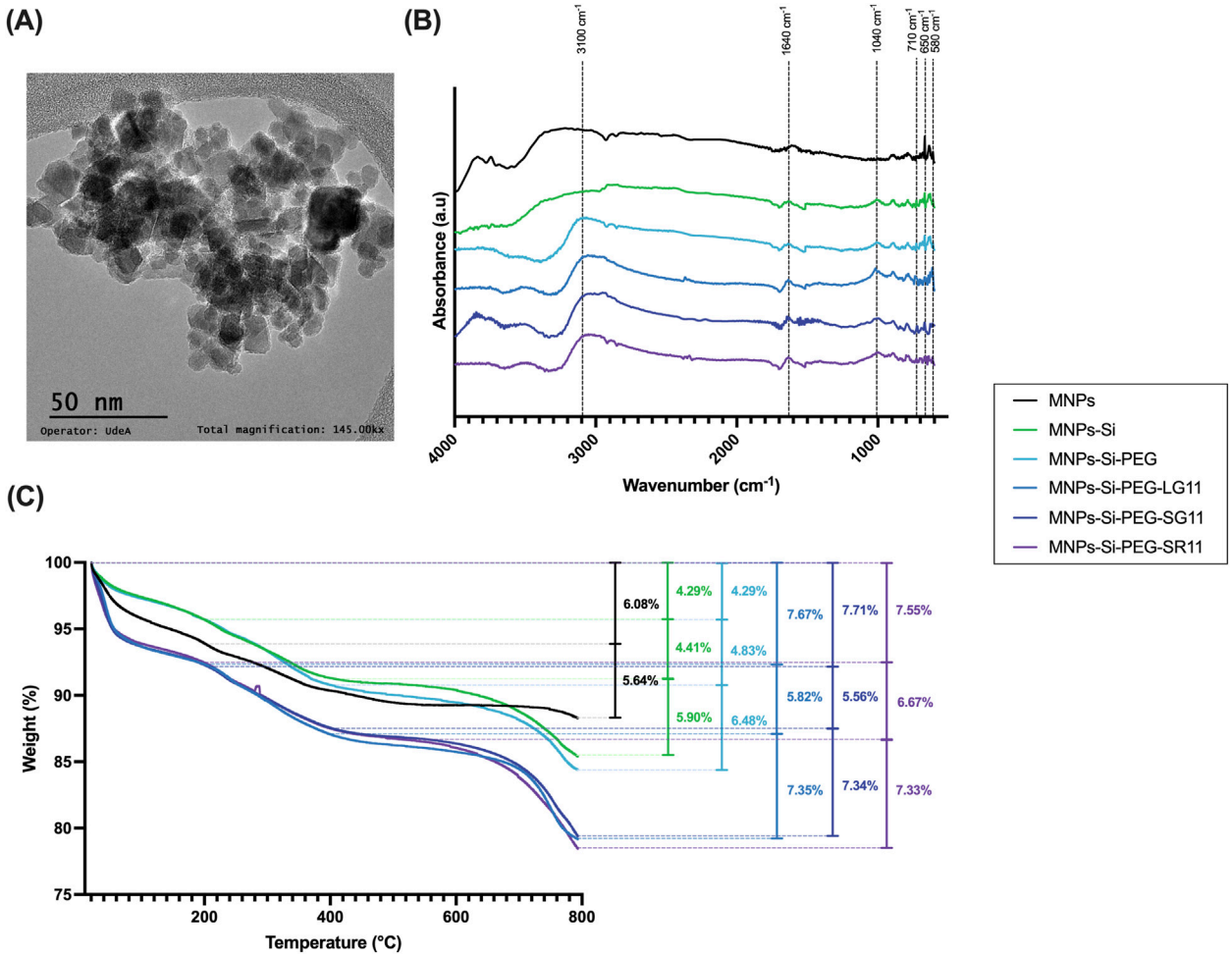

FIGURE 3
Physicochemical characterization of the nanobioconjugates. **(A)** Microscopic characterization of bare MNPs analyzed through TEM at 145 kX, **(B)** FTIR spectra, and **(C)** TGA analysis.

bilayer of cell membranes, which can facilitate cell penetration through direct translocation mechanisms rather than energy-dependent pathways (Gomez et al., 2010). The peptides also exhibit high hydrophobicity and a high isoelectric point (pI). An *in silico* study showed that short peptides with low hydrophobicity and low pI are tended to have the lowest uptake (Matsumoto et al., 2015). Therefore, the high hydrophobicity and high pI values of these peptides suggest effective cell uptake, as hydrophobic interactions play a significant role in crossing cell membranes.

The hydrophobic moment (μH) of a peptide measures its amphipathicity and is an important factor in peptide-mediated membrane disturbance. Peptide-induced membrane leakage tends to be proportional to μH. Therefore, minimizing μH is desirable to reduce CPP-induced plasma membrane damage (Hällbrink et al., 2001). Peptides with high μH (~0.391 and above) show high lytic activity, while those with a low μH (~0.272 and below) exhibit minimal cytotoxicity (Chen et al., 2017). The low μH values for LG11, SG11, and SR11 indicate that these peptides are less likely to cause membrane disturbance or cytotoxicity, which is beneficial for maintaining cell viability while ensuring efficient internalization. The Boman index represents the potential of a peptide to bind to membranes or other proteins. A high Boman index (>2.48) indicates high binding potential, while a low Boman index (≤1) suggests fewer side effects and lower toxicity to mammalian cells (Boman, 2003). The low Boman index values for these peptides suggest that they are less likely to bind nonspecifically to proteins, reducing the risk of off-target effects. These properties enhance the safety and specificity of the peptides for biomedical applications.

Physicochemical characterization of the nanobioconjugates

Physicochemical characterizations of the evaluated nanobioconjugates are presented in Figure 3, while results for the comparative nanobioconjugates with peptides RD10, MS12, and BUFII can be found in the Supplementary Figure S2. Among the parameters influencing the efficacy of nanoparticle-based bioactive molecule delivery systems, nanoparticle size plays a crucial role in determining their performance *in vitro* and *in vivo* for biomedical applications. Properties affected by nanoparticle size include superparamagnetism, toxicity, protein adsorption on the surface, cellular internalization processes, targeted drug delivery, biodistribution, surface reactivity, and tissue marking (Ortega and Reguera, 2019; Montiel Schneider et al., 2022; Petrov and Chubarov, 2022; Nica et al., 2023). TEM was employed to study the morphology and crystalline structure of the bare nanoparticles (Figure 3A). The image illustrates monocrystalline MNPs with uniform sizes and shapes, consistent with previous studies on magnetic nanoparticles (Deng et al., 2005; Krispin et al., 2012; Nguyen et al., 2021).

Surface modifications of magnetite nanoparticles were confirmed using Fourier transform infrared (FTIR) spectroscopy. Figure 3B and Supplementary Figure S2A show the FTIR spectra for the bare MNPs and all the nanobioconjugates. Common peaks at 580 cm^{-1} and 650 cm^{-1} across all spectra can be attributed to the vibration of the Fe-O bond in iron oxide (Cuellar et al., 2018; Perez et al., 2019; Lopez-Barbosa et al., 2020; Rangel-Muñoz et al., 2020). Silanization was confirmed by the presence of the Si-O stretching vibration at 1,040 cm^{-1} and the C-H bending peak at 710 cm^{-1}, indicating successful functionalization with APTES (Cuellar et al., 2018; Perez et al., 2019; Lopez-Barbosa et al., 2020; Rangel-Muñoz et al., 2020). During the PEGylation process, glutaraldehyde was used as a crosslinker, forming imide bonds with the silanized nanoparticles and the PEG molecule (see step 3 of Figure 2). The strong absorption band at 3,100 cm^{-1} corresponds to N–H stretching vibrations associated with amines (Eckel et al., 2001; Ferreira et al., 2022). For peptide immobilization, the zero-length crosslinkers EDC and NHS were employed to form an amide bond between the amino end of the PEGylated nanoparticles and the C-terminal of the peptide (see step 4 of Figure 2). The peak observed at 1,640 cm^{-1} corresponds to amide I, confirming the successful immobilization of the peptides on the nanoparticle surface (Cuellar et al., 2018; Perez et al., 2019).

The secondary structure of the peptides with the motif and the comparative peptides was predicted using PEP-FOLD3 (Thevenet et al., 2012; Shen et al., 2014; Lamiable et al., 2016) (Supplementary Figures S3A, C, E, G, I, K). To ensure that immobilization on nanoparticles did not induce significant structural changes in the peptide, the second derivative of FTIR was analyzed between the wavelengths 1,550 cm^{-1} and 1750 cm^{-1} (blue box) (Supplementary Figures S3B, D, F, H, J, L). These peptide predictions guided the analysis of the second derivative and the determination of the secondary structures of both the free peptides and the peptides after immobilization. LG11 exhibited random coil structures in the center (C4 to G7) observed at 1,651 cm^{-1} (Barth, 2007; Kong and Yu, 2007; Lewis et al., 2013) and beta-sheet structures at the ends, observed at 1,696 cm^{-1} (Kumosinski and Farrell, 1993; Jackson and Mantsch, 1995; Kong and Yu, 2007; Lewis et al., 2013; De Meutter and Goormaghtigh, 2021). After immobilization, the peak for the random coils shifted to 1,655 cm^{-1}, while the beta-sheet peak remained unchanged. SG11 displayed random coil structures throughout its sequence, observed at 1,650 cm^{-1} (Barth, 2007; Kong and Yu, 2007; Lewis et al., 2013). After immobilization, this peak shifted to 1,656 cm^{-1}. SR11 exhibited random coil structures at the ends (S1 to G2 and L7 to C10), observed at 1,676 cm^{-1} (Barth, 2007; Kong and Yu, 2007; Lewis et al., 2013), and an alpha-helix structure in the center (C3 to G6), observed at 1,658 cm^{-1} (Jackson and Mantsch, 1995; Barth, 2007; Kong and Yu, 2007). After immobilization, the random coil peak shifted to 1700 cm^{-1}, while the alpha-helix peak shifted to 1,655 cm^{-1}.

For the comparative peptides, RD10 showed random coil structures throughout its entire sequence, observed at 1,657 cm^{-1} (Barth, 2007; Kong and Yu, 2007; Lewis et al., 2013). After immobilization, this peak remained unchanged. MS12 exhibited alpha-helix structures from F2 to L10, observed at 1,650 cm^{-1} (Jackson and Mantsch, 1995; Barth, 2007; Kong and Yu, 2007). After immobilization, the peak shifted to 1,655 cm^{-1}. Finally, BUFII displayed alpha-helix structures at the ends (R2 to R5 and V12 to L19), observed at 1,650 cm^{-1} (Jackson and Mantsch, 1995; Barth, 2007; Kong and Yu, 2007), and random coil structures in the center (A6 to P11), observed at 1,673 cm^{-1} and 1,680 cm^{-1} (Barth, 2007; Kong and Yu, 2007; Lewis et al., 2013). After immobilization, the alpha-helix peak shifted to 1,658 cm^{-1}, while the random coil peak shifted to 1,685 cm^{-1}. Overall, no significant changes were observed in the secondary structures of the peptides after immobilization.

The surface modifications of the MNPs were also assessed via TGA (Figure 3C; Supplementary Figure S2B) to verify the successful immobilization, the immobilization efficiencies of the attached molecules, and the thermal stability of the nanobioconjugates. TGA is widely used in the characterization of biomaterials (Loganathan et al., 2017; Seifi et al., 2020) that can be employed to verify the successful immobilization and efficiency of molecule attachment on the nanoparticle surface (Almaghrabi et al., 2023). For the bare nanoparticles, two weight losses were observed, whereas three weight losses were noted for the nanobioconjugates due to surface functionalization, consistent with other studies (Cuellar et al., 2018; Perez et al., 2019; Lopez-Barbosa et al., 2020; Rangel-Muñoz et al., 2020). The first weight loss, occurring between 24°C and 200°C, ranged from 4.29% to 7.71% and is associated with the dehydration of the sample (loss of physically adsorbed water on the nanobioconjugate surface). The second weight loss, from 200°C to 400°C, ranged from 4.41% to 10.4% and can be attributed to the desorption of physically adsorbed organic and inorganic compounds that remain from the synthesis and immobilization processes. The third weight loss, occurring from 400°C to 800°C, ranged from 5.90% to 7.35% and corresponds to the detachment of the APTES, PEG, and peptide molecules from the nanoparticle. Supplementary Table S1 summarizes the peptide immobilization efficiencies for each nanobioconjugate, with all efficiencies exceeding 50%. Overall, the synthesized nanobioconjugates demonstrate substantial thermal stability below 400°C, indicating their safety at physiological temperatures.

Figures 4A–D and Table 2 show the average hydrodynamic diameters of each nanobioconjugate in various media, while Supplementary Figures S4A–C and Supplementary Table S2

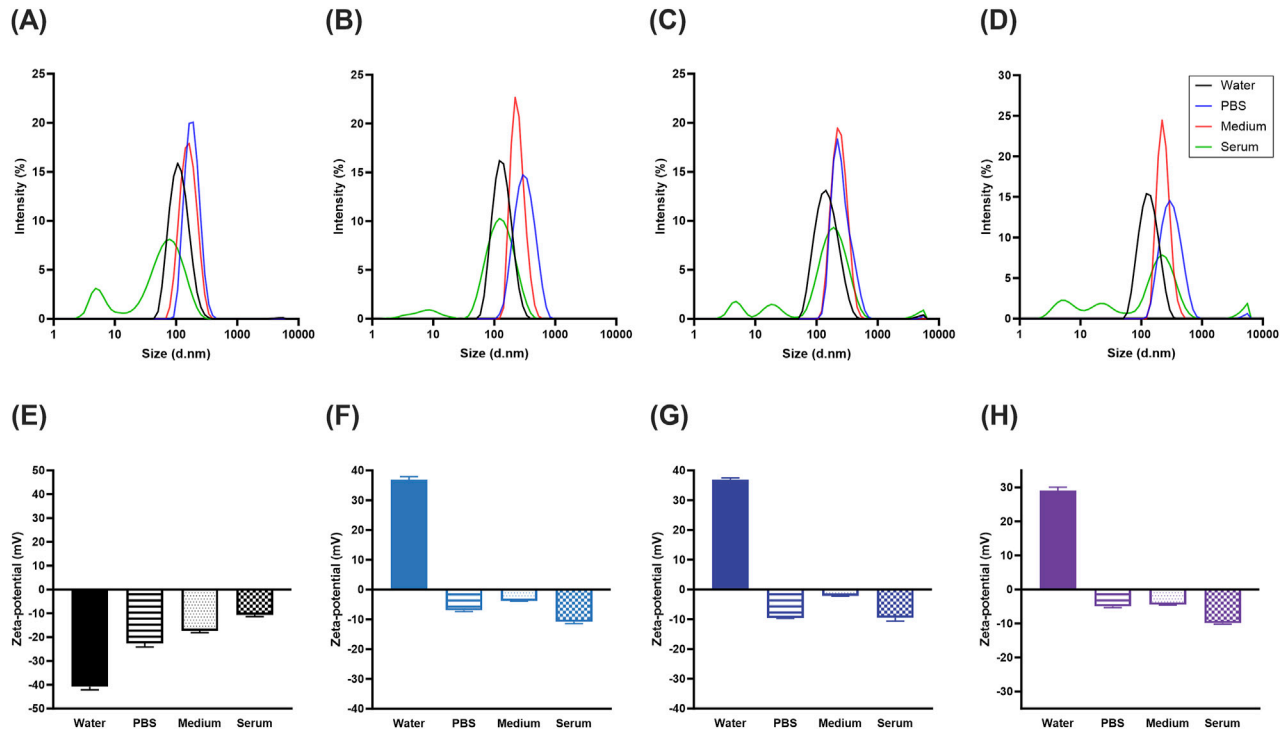

FIGURE 4
DLS intensity plots of comparative nanobioconjugates dispersed in water at pH 7.4 (water), PBS 1X (PBS), DMEM (medium), and DMEM + 10% (v/v) FBS (serum) for the **(A)** bare MNPs, **(B)** LG11, **(C)** SG11, and **(D)** SR11 nanobioconjugates. Zeta potential measurements of the nanobioconjugates under the same conditions for the **(E)** bare MNPs, **(F)** LG11, **(G)** SG11, and **(H)** SR11 nanobioconjugates.

present the data for the comparative nanobioconjugates. In water, the bare MNPs exhibited an average hydrodynamic diameter of 109.9 ± 1.106 nm, while both the designed and comparative nanobioconjugates had average diameters below 160 nm. The results demonstrate a progressive increase in hydrodynamic diameter with each functionalization step, including silanization, PEGylation, and peptide immobilization.

In water, all nanobioconjugates exhibited smaller diameters compared to those in PBS and medium, likely due to water providing a more stable environment that enhances the nanoparticle surface charge (Wiogo et al., 2011). Conversely, the high ionic strength of PBS and medium suppresses the electric double layer and reduces electrostatic repulsion, promoting nanoparticle agglomeration (Wiogo et al., 2011; Mbeh et al., 2015). Interestingly, although medium has a higher salt content than PBS, which would typically result in greater agglomeration, most nanobioconjugates exhibited a size reduction when transitioning from PBS to medium. In serum, multiple peaks were observed, likely representing agglomerates of various sizes and the coexistence of protein monomers and aggregates. The presence of smaller nanoparticle agglomerates may be attributed to structural interactions between the immobilized peptides and serum proteins, which bind to the peptide surfaces and stabilize the nanoparticles—a phenomenon known as the protein corona effect (Mbeh et al., 2015). Serum components such as globulin and transferrin are known to interact with nanoparticles, helping prevent further agglomeration (Ji et al., 2010; Yu et al., 2014).

The polydispersity index (PDI) is a dimensionless number used to quantify the uniformity of size distribution among molecules or particles in a sample. PDI values above 0.7 typically indicate high polydispersity, making the sample unsuitable for analysis by DLS (Danaei et al., 2018). In contrast, PDI values below 0.2 are considered optimal for polymer-based nanomaterials (Lahiri et al., 2017; Danaei et al., 2018). In this study, higher PDI values (above 0.2) were primarily observed in nanobioconjugates dispersed in medium and serum. The elevated PDI in serum, along with a broad particle size distribution, can be attributed to the coexistence of Bovine Serum Albumin (BSA) monomers and agglomerates (Orts-Gil et al., 2011; Hondow et al., 2012). All nanobioconjugates evaluated in water exhibited PDI values below 0.185, while most nanobioconjugates in PBS and medium had PDI values under 0.2, indicating a narrow size distribution and good nanoparticle homogeneity. Interestingly, it was observed that when the surface charge approached neutrality, the hydrodynamic size increased due to agglomeration (Mbeh et al., 2015). Maintaining low PDI values is crucial for ensuring consistent physical and chemical properties, reproducibility, stability, and efficacy of nanocarriers. These characteristics suggest a wide range of potential applications in the biomedical field, including drug delivery (Anik et al., 2021), cellular internalization processes (Zhao et al., 2011), intravenous injection (Kudr et al., 2017), targeted therapy (Fatima et al., 2021), biosensors (Rocha-Santos, 2014), and others.

The zeta potential is a physical property that allows for the determination of the surface charge of particles and quantify the magnitude of the electrostatic repulsion or attraction between

TABLE 2 DLS and zeta potential test results for the nanobioconjugates, showing nanoparticle size, polydispersity index, and surface charge in water at pH 7.4 (water), PBS 1X (PBS), DMEM (medium), and DMEM + 10% (v/v) FBS (serum).

Solution	Nanobioconjugate	Average diameter (nm)	Polydispersity index	Zeta-potential (mV)
Water	MNPs	109.9 ± 1.106	0.168 ± 0.017	−40.8 ± 1.350
	MNPs-Si-PEG	120.8 ± 1.464	0.149 ± 0.001	29.70 ± 0.777
	MNPs-Si-PEG-LG11	128.2 ± 0.656	0.141 ± 0.029	36.80 ± 1.10
	MNPs-Si-PEG-SG11	137.5 ± 0.322	0.166 ± 0.019	36.93 ± 0.643
	MNPs-Si-PEG-SR11	126.0 ± 1.550	0.133 ± 0.003	29.08 ± 0.977
PBS	MNPs	198.0 ± 17.76	0.235 ± 0.026	−22.7 ± 1.44
	MNPs-Si-PEG-LG11	298.6 ± 28.53	0.149 ± 0.032	−6.95 ± 0.437
	MNPs-Si-PEG-SG11	276.4 ± 6.766	0.235 ± 0.085	−9.62 ± 0.0666
	MNPs-Si-PEG-SR11	294.8 ± 22.79	0.160 ± 0.037	−4.96 ± 0.405
Medium	MNPs	160.7 ± 20.02	0.205 ± 0.014	−17.3 ± 0.839
	MNPs-Si-PEG-LG11	272.0 ± 12.16	0.236 ± 0 .038	−3.78 ± 0.111
	MNPs-Si-PEG-SG11	244.3 ± 18.25	0.194 ± 0.025	−2.135 0.134
	MNPs-Si-PEG-SR11	300.5 ± 3.180	0.319 ± 0.035	−4.50 ± 0.0608
Serum	MNPs	83.53 ± 1.328[a]	0.653 ± 0.055	−10.7 ± 0.681
		6.953 ± 2.795[b]		
	MNPs-Si-PEG-LG11	141.4 ± 5.380[a]	0.534 ± 0.051	−10.8 ± 0.600
		9.642 ± 3.125[b]		
	MNPs-Si-PEG-SG11	211.1 ± 9.292[a]	0.724 ± 0.005	−9.52 1.11
		8.939 ± 6.453[b]		
	MNPs-Si-PEG-SR11	233.4 ± 8.584[a]	0.930 ± 0.122	−9.87 ± 0.302
		7.0245 ± 2.776[b]		

[a]Refers to the first (maximum) peak.
[b]Refers to the second peak.

molecules in a suspension. It provides valuable insights into the long-term stability of colloidal systems by indicating whether molecules are likely to disperse, aggregate, or flocculate (Zavisova et al., 2019). Large zeta potentials are generally defined as values greater than +25 mV or less than −25 mV, indicating that the molecules tend to repel each other and avoid agglomeration, coagulation or flocculation (Bhattacharjee, 2016; Zavisova et al., 2019). Figures 4E–H and Table 2 show the zeta potential measurements obtained for nanobioconjugates dispersed in different media. For the MNPs in water, a negative surface charge of −40.8 ± 1.350 mV was observed, consistent with values reported (Li et al., 2022). After the PEGylation of the nanoparticles, the surface charge shifted to positive, with a value of +29.70 ± 0.777 mV. This change in surface charge is consistent with previous studies confirming that PEG is a polycationic polymer (Chen et al., 2013). After peptide immobilization, the zeta potentials for the LG11-, SG11-, and SR11-nanobioconjugates were +36.80 ± 1.10 mV, +36.93 ± 0.643 mV, and +29.08 ± 0.977 mV, respectively. These results indicate that the nanobioconjugates in water achieved optimal zeta potential values, promoting molecular repulsion and system stability.

In contrast, in solutions such as PBS, medium, and serum, the zeta potentials of all nanobioconjugates and bare MNPs were negative, consistent with previous studies (Chircov et al., 2023; Portilla et al., 2023). The negative charge of the nanobioconjugates and bare MNPs in PBS can be attributed to the adsorption of phosphate groups ($HPO_4^{2-}/H_2PO_4^-$) and bicarbonate (HCO_3^-) onto the nanoparticle surfaces (Kaewsichan et al., 2011; Zhu et al., 2020). Similarly, in medium, anions such as sulfates (SO_4^{2-}), bicarbonate, and phosphate groups adsorb onto the particles, imparting a negative charge (Harjo et al., 2019; Bița et al., 2022). In serum, the same anions are present, along with BSA, which is negatively charged at physiological pH. The interaction and adsorption of BSA onto the nanoparticle surfaces further explain the negative charge of the nanobioconjugates in serum (Fologea et al., 2007). Compared to water, the zeta potentials in PBS, medium, and serum were generally lower due to the higher ionic strength of these solutions, which reduces the thickness of the electric double layer, decreases electrostatic repulsion, and facilitates particle interactions (Choi et al., 2004). The differences in zeta potential between medium and serum likely arise from the varying protein content in these solutions, with BSA adsorption altering both the surface charge and zeta potential of the nanoparticles. A similar

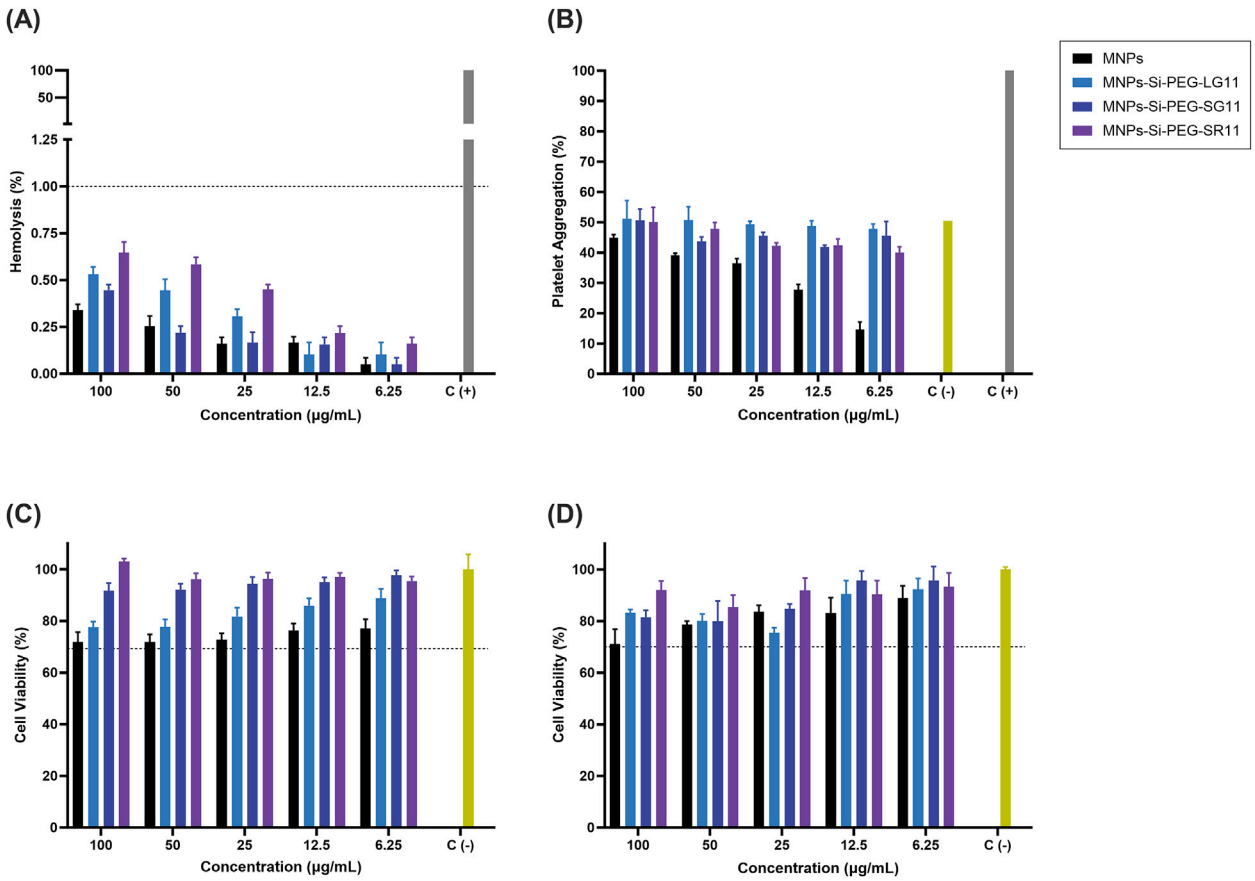

FIGURE 5
Biocompatibility and cell viability of nanobioconjugates. **(A)** Hemolytic effect assessment, using PBS 1X as the negative control and Triton X-100 (10% v/v) as the positive control. **(B)** Platelet aggregation analysis, with PBS 1X as the negative control and Thrombin (9U) as the positive control. Cell viability of Vero cells after nanobioconjugate exposure for **(C)** 24 h and **(D)** 48 h. Non-treated cells were employed as positive control.

trend was observed for the comparative nanobioconjugates of peptides RD10, MS12, and BUFII, with positive zeta potentials in water and negative zeta potentials in PBS, medium, and serum. These results are presented in Supplementary Figures S4D–F and Supplementary Table S2.

Biocompatibility studies

Figures 5A, B illustrate the hemolytic activity and platelet aggregation effects of the nanobioconjugates, respectively. All treatments exhibited average hemolytic activity below 1%, and no significant platelet aggregation was observed compared to the PBS control. Generally, the nanobioconjugates showed an increase in platelet aggregation compared to the bare MNPs, with the LG11-nanobioconjugate displaying slightly more aggregation among the designed nanobioconjugates. Additionally, a platelet uptake assay was developed to assess whether nanoparticles were internalized by platelets (see Supplementary Figure S5). The results indicated that peptide immobilization slightly enhanced nanoparticle uptake by platelets. MNPs showed an uptake of 6.12%, while the LG11-, SG11-, and SR11-nanobioconjugates exhibited uptakes of 12.76%, 14.27%, and 13.84%, respectively. Although the nanobioconjugates demonstrated increased platelet uptake, these differences were not statistically significant.

Previous studies have shown that CPPs can activate surface receptors on platelet membranes, particularly at higher concentrations where this mechanism is amplified (Ruseska and Zimmer, 2020). This suggests that the LFVCR motif may contain amino acids that influence this process. Arginine, a precursor to nitric oxide (NO), has been reported to play a dual role depending on the local environment, either inhibiting platelet aggregation via NO production or supporting aggregation through other pathways (Gambaryan and Tsikas, 2015; Gawrys et al., 2020). It is hypothesized that in the LG11-nanobioconjugate, arginine might be more exposed and interact more with platelets, leading to the slight increase in platelet aggregation observed. However, the overall influence of the LFVCR motif on platelet aggregation appears to be minimal. Other amino acids in the motif, such as leucine, phenylalanine, and valine, have been studied for their anticoagulant effects (Xu et al., 2020; Grigorieva et al., 2023; Qin et al., 2023). Additionally, cysteine residues might influence antiplatelet adhesion through the HNP-1 pathway, though their exact role under normal physiological conditions remains unclear (McDaniel et al., 2019). Overall, the results indicate that the nanobioconjugates are suitable for intravenous administration

10.3389/fbioe.2024.1450694

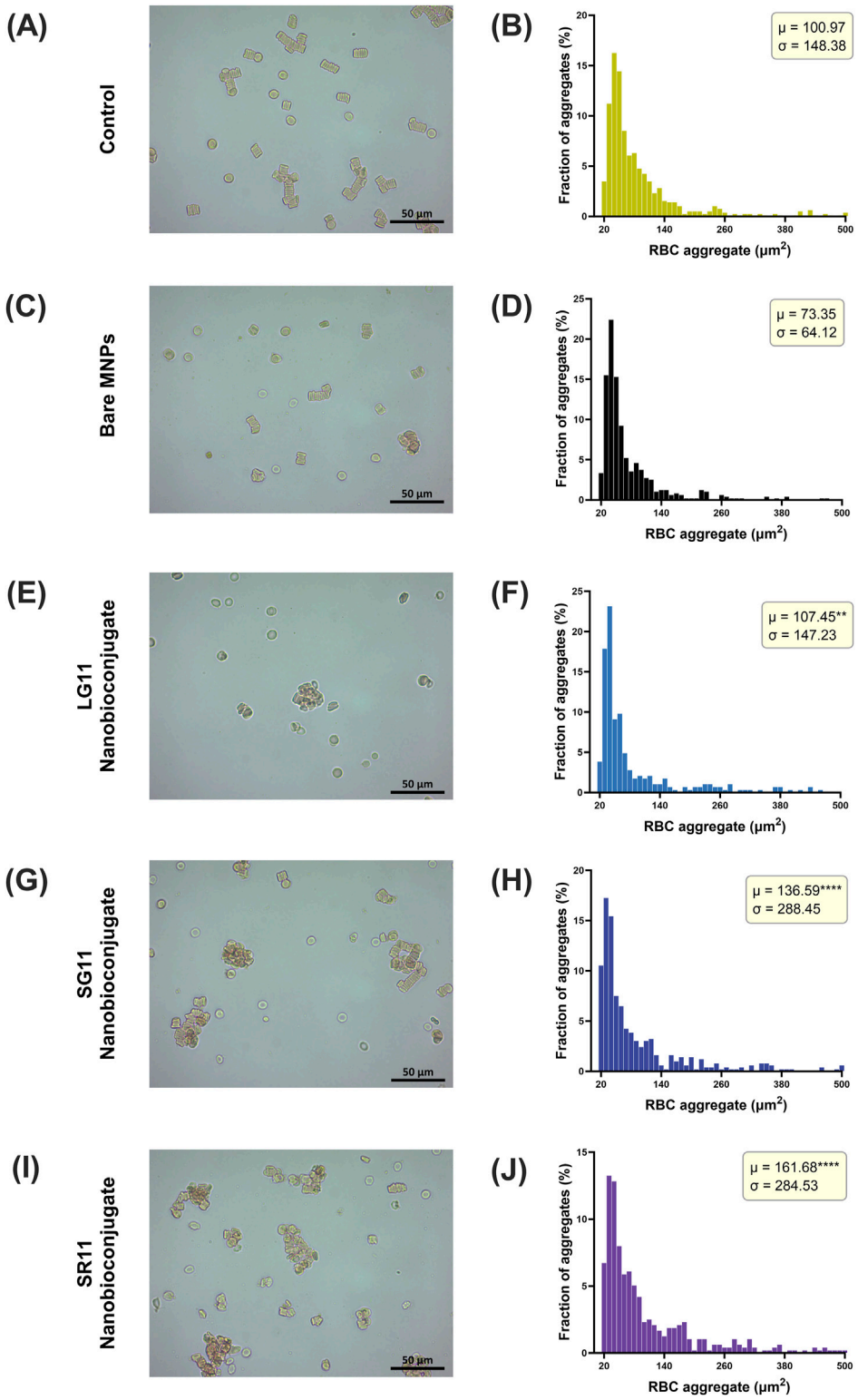

FIGURE 6
Relative size distribution of RBC aggregates observed at 40× magnification using conventional optical microscopy under **(A)** normal conditions and upon exposure to **(C)** Bare MNPs, **(E)** LG11, **(G)** SG11, and **(I)** SR11 nanobioconjugates. Corresponding size distribution histograms are provided for (B) normal conditions and for exposure to **(D)** Bare MNPs, **(F)** LG11, **(H)** SG11, and **(J)** SR11 nanobioconjugates. The symbol * corresponds to a statistically significant difference with a p-value in the range of $0.01 \leq$ p-value ≤ 0.05, ** to a statistically significant difference with a p-value in the range of $0.001 \leq$ p-value <0.01, *** to p-value in the range of $0.0001 \leq$ p-value ≤ 0.001 and **** to p-value < 0.0001.

with a low risk of causing thrombosis. According to the ISO 10993–4:2018 standard, these findings underscore the high hemocompatibility of the nanobioconjugates (International Organization for Standardization, 2018).

Figures 5C, D show the cytocompatibility results of the nanobioconjugates on Vero cells over 24 and 48 h of exposure, respectively. The results indicate that the nanobioconjugates exhibited significantly higher cell viability compared to the bare MNPs, suggesting that the peptides contribute substantially to the biocompatibility of the MNPs. These findings align with the predictions of the peptides' physicochemical properties. The low μH values predicted for the designed peptides indicated that these peptides are less likely to cause membrane disturbance or cytotoxicity (Hällbrink et al., 2001), a characteristic confirmed by the cytocompatibility results. For both exposure times, the LG11-nanobioconjugate exhibited the lowest cell viability percentages compared to the other nanobioconjugates. This reduction in cell viability can be attributed to a high uptake of the nanobioconjugate by the cell line (Cuellar et al., 2018; Perez et al., 2019; Cifuentes et al., 2023). This result will be analyzed further in the next section. Overall, all vehicles showed cell viability percentages above 70%, qualifying them as non-cytotoxic according to the ISO 10993–5: 2009 standard (ISO, 2009). These findings confirm the excellent biocompatibility of the nanobioconjugates and highlight their potential for safe cellular uptake.

The cytotoxic effects of Rhodamine B-labeled nanobioconjugates were assessed at 0.5 and 4 h, with comparisons to unlabeled nanobioconjugates to evaluate their impact on cell viability in the cellular internalization assays (Supplementary Figure S6). The results showed that labeling with Rhodamine B reduce the viability in Vero cells at both intervals. At the 0.5-h mark, viability decreased in a range of 3.29%–20.43%, and at the 4-h mark, viability decreased in a range of 7.61%–19.05%. The cytotoxic effects observed are consistent with the known properties of this fluorescent dye, which affects various cell lines, including Vero cells (Serbian et al., 2020; Shi et al., 2020). Despite these effects, cell viability of labeled nanobioconjugates remained above 70%.

Figure 6 illustrates the evaluation of the procoagulant activity of bare MNPs and nanobioconjugates. The general results reveal that erythrocytes (RBCs) incubated with nanobioconjugates tend to form aggregates of irregular size and shape, distinct from those observed in the control and bare MNPs, which exhibited smaller agglomerations. In the control sample and in the presence of bare MNPs, RBCs formed typical rouleaux-shaped aggregates (Figures 6A, C). This phenomenon occurs because RBCs tend to stick together in plasma due to proteins like fibrinogen, which reduce the repulsive forces between cells, allowing RBC stacking (Rampling, 1999; Avsievich et al., 2019). However, these characteristic forms were reduced in RBCs exposed to nanobioconjugates, where larger, irregular agglomerates were observed (Figures 6E, G, I). The size distribution of RBC aggregates is depicted in Figures 6B, D, F, H, J, allowing the determination of mean and standard deviation for aggregate sizes. Notably, the LG11-nanobioconjugate resulted in a mean agglomerate size of 107.45 μm^2, close to that observed under normal conditions (100 μm^2). In contrast, the other nanobioconjugates significantly increased the size of RBC aggregates, with the SG11-nanobioconjugate showing an average size of 136.59 μm^2 and the SR11-nanobioconjugate at 161.68 μm^2. These findings indicate that the peptide with the exposed motif in the LG11-nanobioconjugate induced the least increase in procoagulant activity among the nanobioconjugates. A previous study has demonstrated that MNPs can exhibit procoagulant activity by aggregating and adhering to RBC membranes (Ran et al., 2015). However, in our study, bare MNPs did not show a significant increase in procoagulant activity. A slight increase was observed for the LG11-nanobioconjugate, while a more pronounced increase was found for the SG11 and SR11 nanobioconjugates.

The biocompatibility results compile evidence supporting the nanobioconjugates' potential use in numerous applications and therapies. Their low thrombotic, hemolytic, and cytotoxic potential, along with their procoagulant activity, highlights their suitability for therapeutic use via intravenous administration (Shariatinia, 2021). The absence of cellular injury risk makes these nanocarriers suitable candidates for intracellular drug delivery, facilitating anticancer therapies, delivering anti-inflammatory drugs, and aiding in diagnostic applications by transporting markers for medical imaging (Derakhshankhah and Jafari, 2018). Additionally, various studies have proven that CPPs can assist in treating Central Nervous System disorders. The blood-brain barrier (BBB) is known for its low permeability, standing a significant challenge for drug delivery to the brain. However, biocompatible CPP-based nanocarriers have demonstrated successful transportation of therapeutic agents across the BBB, enabling effective treatment of neurological conditions (Hersh et al., 2022). This capability to cross the BBB and deliver drugs directly to the brain underscores the potential of CPPs in addressing diseases such as Alzheimer's, Parkinson's, and other neurodegenerative disorders, providing a promising avenue for future therapeutic developments (Sharma et al., 2016; Xie et al., 2020).

Cellular internalization pathways and endosomal escape analysis

Confocal microscopy was employed to investigate the cellular uptake mechanisms of the designed nanobioconjugates and MNPs on the Vero cell line. Understanding these processes is crucial for biomedical applications, as it elucidates how molecules of interest enter cells. The energy-dependent process of cellular uptake, known as endocytosis, involves the internalization of external molecules into the cell through the formation of invaginations in the cell membrane (Mayor and Pagano, 2007; Doherty and McMahon, 2009). These internal structures are known as vesicles (or endosomes). Clathrin-mediated endocytosis is the most common endocytic mechanism in all cell types and tissues due to its high availability and adaptability towards recognizing numerous agents (Rueda-Gensini et al., 2020) and has been extensively documented in previous studies as a prevalent route for nanobioconjugate cellular uptake, including iron oxide nanoparticles (IONPs) (Lunov et al., 2011; Luther et al., 2013; Chen et al., 2017).

Figures 7, 8 present the confocal images obtained. These images were used to determine the Pearson Correlation Coefficient (PCC) as an indicator of the nanoparticles' endosomal escape or entrapment. Additionally, these images were utilized to determine

10.3389/fbioe.2024.1450694

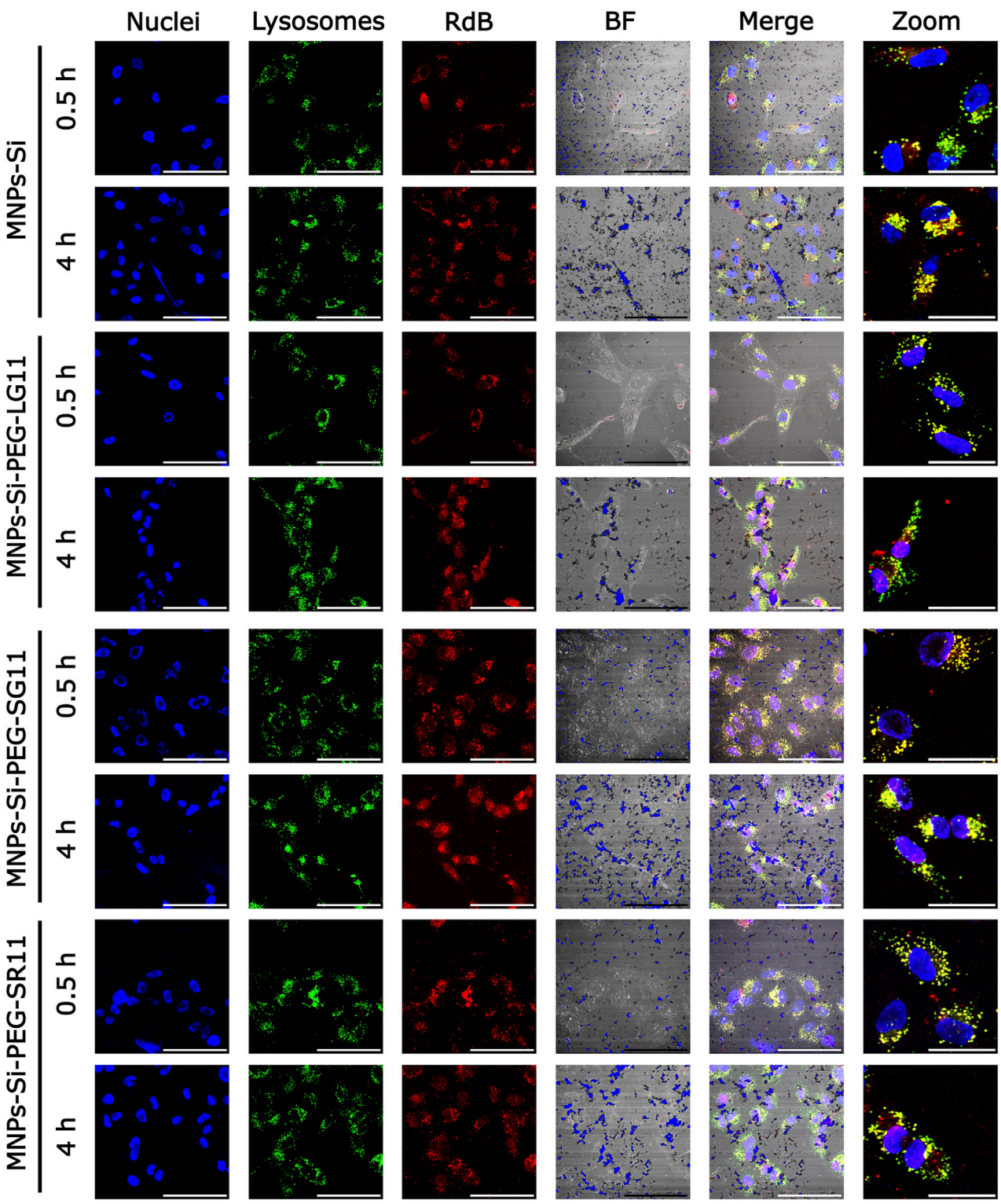

FIGURE 7
Confocal microscopy images for cell internalization and endosomal escape analysis in Vero cells at 0.5 h and 4 h of exposure, without inhibition. Images were captured using a digital zoom on ×20 magnification. The scale bars represent 100 μm for standard images and 50 μm for zoomed images. In all nanobioconjugates, the first three channels show nuclei labeled with Hoechst (blue), lysosomes with Lysotracker Green (green), and nanobioconjugates with Rhodamine-B (red). Yellow areas indicate colocalization between the red and green channels, suggesting lysosomal entrapment.

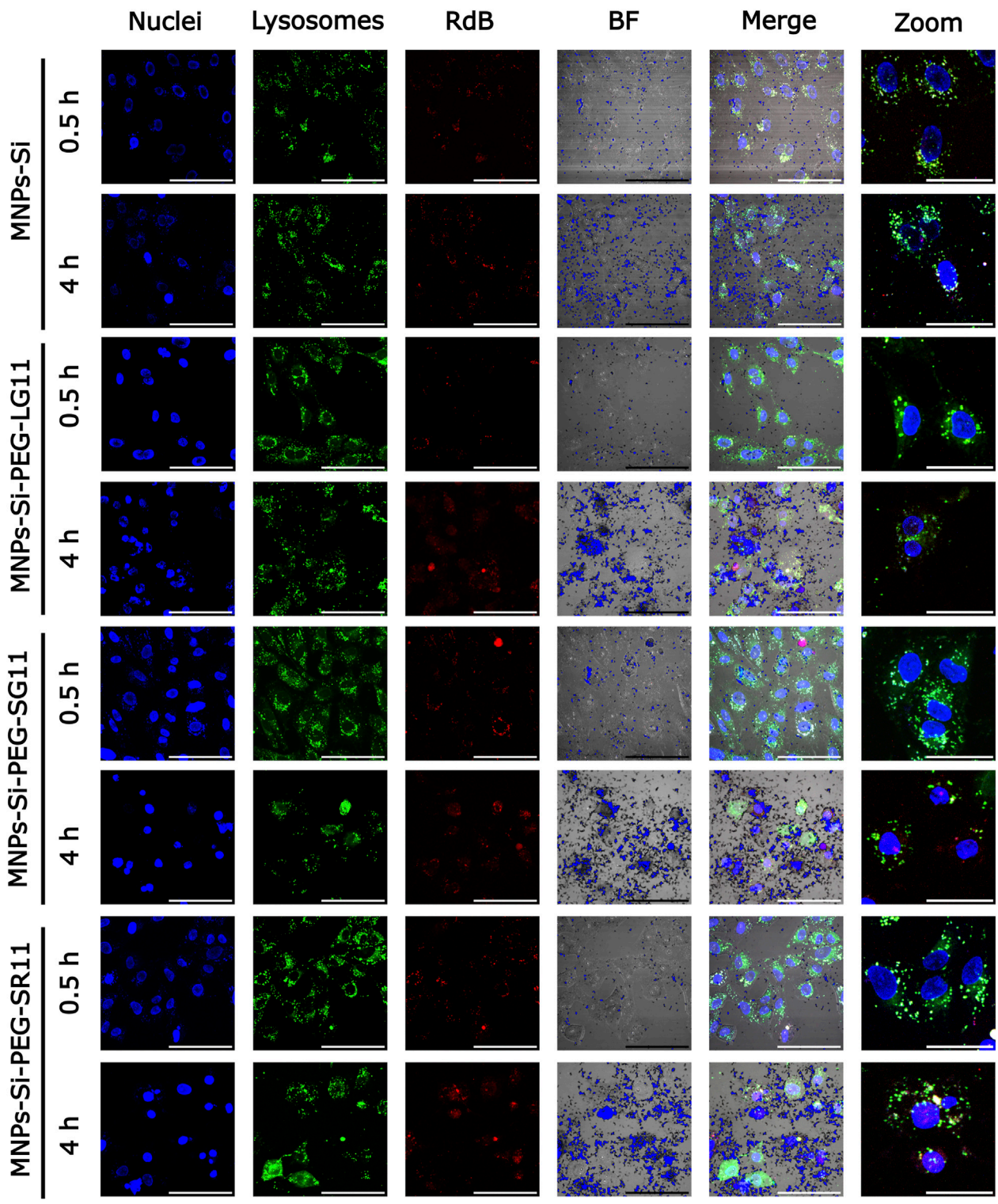

FIGURE 8
Confocal microscopy images for cell internalization and endosomal escape analysis in Vero cells at 0.5 h and 4 h of exposure, with clathrin-mediated endocytosis inhibition. Images were captured using a digital zoom on ×20 magnification. The scale bars represent 100 μm for standard images and 50 μm for zoomed images. In all nanobioconjugates, the first three channels show nuclei labeled with Hoechst (blue), lysosomes with Lysotracker Green (green), and nanobioconjugates with Rhodamine-B (red). Yellow areas indicate colocalization between the red and green channels, suggesting lysosomal entrapment.

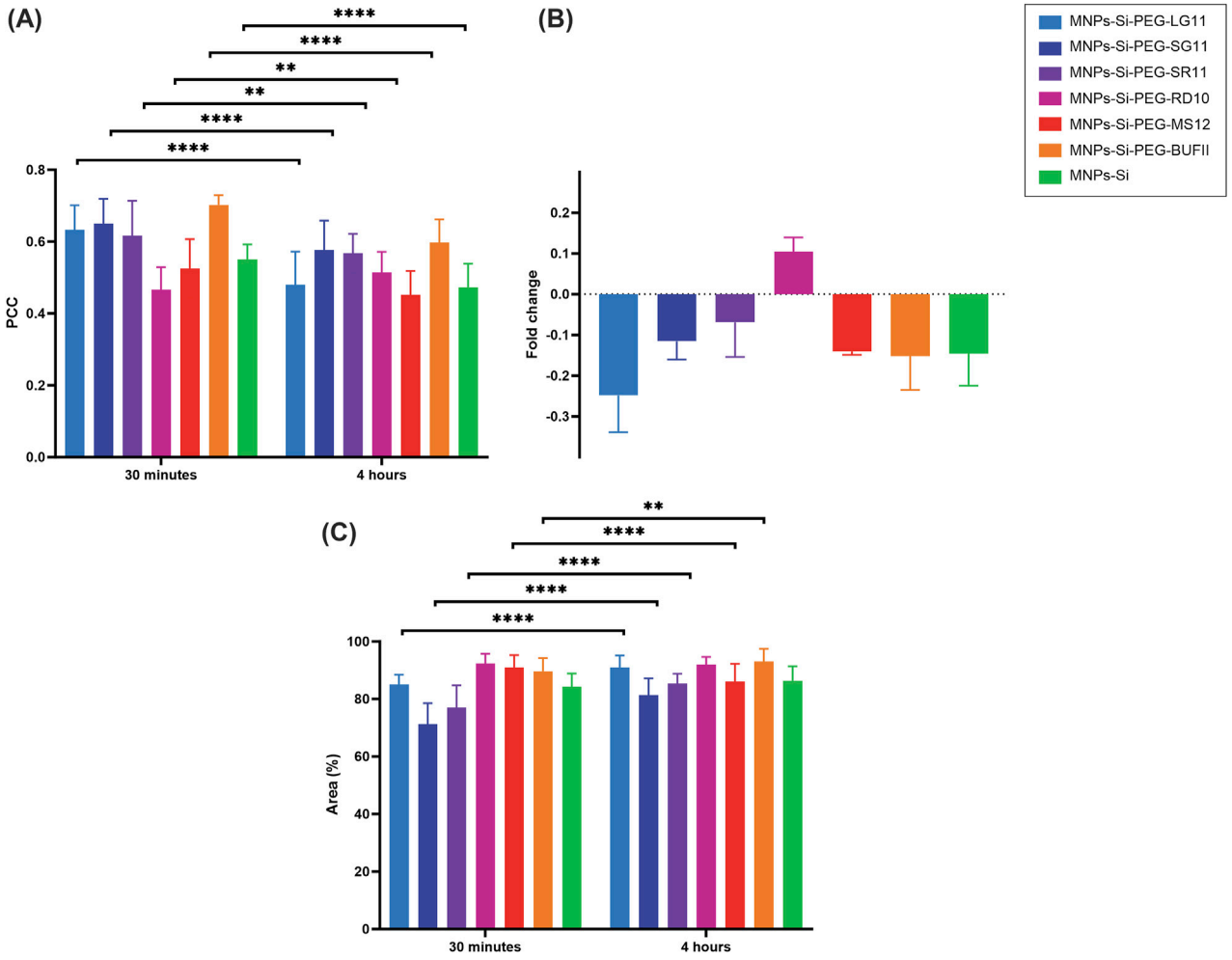

FIGURE 9
Cell-internalization and endosomal escape analysis without inhibition for the designed and comparative nanobioconjugates in Vero cells at 0.5 h and 4 h of exposure. **(A)** Pearson Correlation Coefficient (PCC), where higher values indicate stronger correlation between the red and green channels, suggesting endo/lysosomal entrapment. **(B)** Fold change analysis of the PCC. **(C)** Percentage of intracellular area covered by nanobioconjugates. Statistical significance is denoted as follows: * for p-values between 0.01 and 0.05, ** for p-values between 0.001 and 0.01, *** for p-values between 0.0001 and 0.001, and **** for p-values less than 0.0001.

the percentage of area covered by the nanoparticles, indicating cellular uptake, with and without inhibition, respectively. These results are depicted in Figures 9, 10. Figure 9 illustrates the results for the designed nanobioconjugates with immobilized peptides that allowed modification of the motif position and its exposure (LG11-, SG11-, and SR11-nanobioconjugate), as well as the non-modified MNPs. The performance of the designed nanobioconjugates was compared with nanobioconjugates immobilizing previously reported CPPs (RD10, MS12, and BUFII) (Park et al., 1996; Park et al., 2000; Henao et al., 2022; Ruiz Puentes et al., 2022). Detailed confocal images of the comparative nanobioconjugates are available in Supplementary Figure S7. To facilitate the analysis of endosomal escape, the fold change (Figure 9B) was calculated using the PCC graph (Figure 9A). In this graph, negative values indicate successful endosomal escape, while positive values indicate endosomal entrapment.

The results show that MNPs exhibit endosomal escape, which can be attributed to their surface charge in acidic pH environments. This environment causes the surface charge to become more positive, potentially inducing endosomal escape through electrostatic interactions (Ahmad et al., 2019). The LG11-nanobioconjugate exhibits enhanced endosomal escape compared to the unmodified MNPs and the SG11 and SR11 nanobioconjugates, indicating that the exposure of the LFVCR motif at the free N-terminal enhances the nanovehicle's endosomal escape capabilities. Additionally, the LG11 nanobioconjugate demonstrated higher endosomal escape than nanobioconjugates with the previously reported CPPs: RD10, MS12, and BUFII. This suggests that the motif may facilitate the rupture of the endosomal layer, and the specific motif position in SG11 and SR11 peptides may interfere with the nanoparticles' escape mechanism. It is well-established that positively charged CPPs preferentially bind to negatively charged phospholipids. Notably, the intraluminal lipid bilayers of late endosomes are uniquely enriched with the negatively charged phospholipid bis (monoacylglycero) phosphate (BMP) (Kobayashi et al., 2001; Matsuo et al., 2004). Studies have shown that CPPs can induce

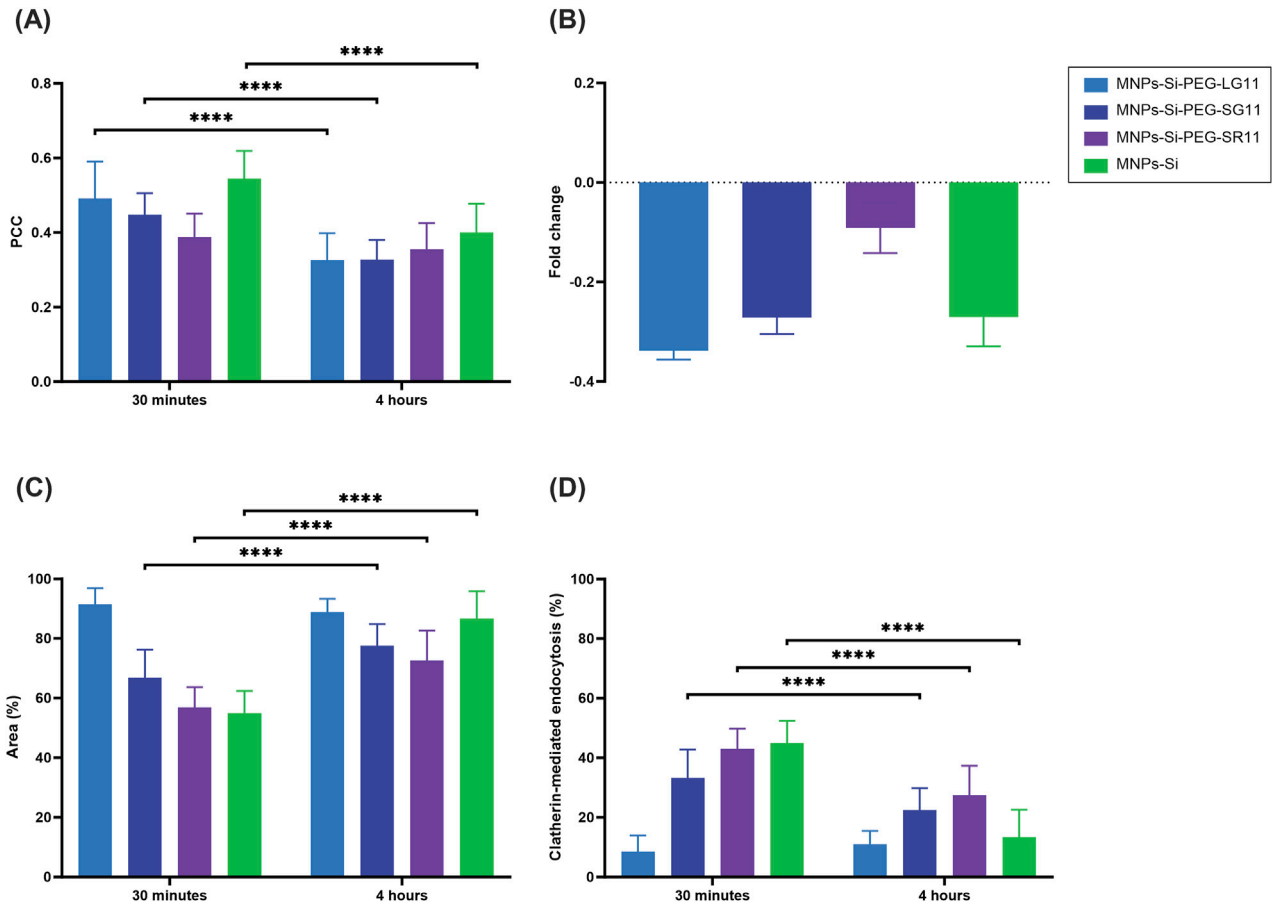

FIGURE 10
Cell-internalization and endosomal escape analysis with clathrin-mediated endocytosis inhibition of the designed nanobioconjugates in Vero cells at 0.5 h and 4 h of exposure. **(A)** Pearson Correlation Coefficient (PCC), where higher values indicate stronger correlation between the red and green channels, suggesting endo/lysosomal entrapment. **(B)** Fold change analysis of the PCC. **(C)** Percentage of intracellular area covered by nanobioconjugates. **(D)** Percentage of cellular uptake via clathrin-mediated endocytosis. The symbol * corresponds to a statistically significant difference with a p-value in the range of $0.01 \leq$ p-value ≤ 0.05, ** to a statistically significant difference with a p-value in the range of $0.001 \leq$ p-value <0.01, *** to p-value in the range of $0.0001 \leq$ p-value ≤ 0.001 and **** to p-value < 0.0001.

membrane leakage in a BMP concentration-dependent manner, with greater activity at pH 5.5 (endosomal pH) than at physiological pH (Appelbaum et al., 2012). Other research supports that CPPs may undergo conformational changes due to the acidification inside the endosomes, which can destabilize the endosomal membrane bilayer (Erazo-Oliveras et al., 2012; Liang and Lam, 2012).

The fold change also indicated that the endosomal escape ability of SG11 and SR11 nanobioconjugates was lower than that of the MNPs. The differential effects of the SG11 and SR11 nanobioconjugates compared to the LG11 nanobioconjugate are important to acknowledge. The reduction in endosomal escape observed with SG11 and SR11 nanobioconjugates may be due to the distribution of their residues, which occlude the motif hypothesized to aid in endosomal escape. Comparing these results with those of the RD10 nanobioconjugate, which does not promote endosomal escape and tends to remain entrapped within endosomes to a greater extent, suggests that the absence of an exposed motif in SG11 and SR11 nanobioconjugates reduces the efficacy of endosomal escape, aligning their behavior more closely with the RD10 nanobioconjugate.

The cell covered area percentage for each conjugate is presented in Figure 9C. The results indicate that the designed nanobioconjugates showed an increase in cell uptake by Vero cells between 30 min and 4 h of exposure. At the 4-h mark, the LG11-nanobioconjugate, which has the most exposed motif, exhibited the highest internalization compared to SG11 and SR11 nanobioconjugates, which did not surpass the internalization level of the MNPs. Although the LG11-nanobioconjugate had lower internalization at 30 min, it significantly increased after 4 h, surpassing the MS12-nanobioconjugate and approaching the levels of the RD10 and BUFII nanobioconjugates. The initially lower uptake of the LG11-nanobioconjugate and the higher uptake of the comparative nanobioconjugates at 30 min can be associated with the fact that cationic nanoparticles generally exhibit higher uptake than anionic nanoparticles, due to repulsive forces between the anionic particles and the cell membrane (Karlsson et al., 1999). Cationic nanoparticles can initially utilize energy-independent mechanisms for cellular uptake (Rueda-Gensini et al., 2020), facilitated by electrostatic interactions between positively charged amino acids and negatively charged sulfonated glycoproteins, which destabilize the cell

membrane (Fröhlich, 2012). However, cationic particles can also enter cells via energy-dependent pathways (Rueda-Gensini et al., 2020). On the other hand, anionic nanoparticles primarily rely on energy-dependent mechanisms such as macropinocytosis, clathrin-mediated endocytosis, and caveolin-mediated endocytosis for internalization (Harush-Frenkel et al., 2007; Martín et al., 2011; Neves-Coelho et al., 2017; Sousa de Almeida et al., 2021). The significant increase in LG11-nanobioconjugate uptake after 4 h suggests that energy-dependent pathways are slower than energy-independent mechanisms, leading to delayed but substantial uptake of the anionic LG11-nanobioconjugate. The authors hypothesized that this slower uptake might be associated with the remarkable potential of the nanobioconjugate for endosomal escape.

The inhibition of the clathrin-mediated route was assessed for the nanobioconjugates to determine the effect of motif position on cellular uptake and endosomal escape, as clathrin-mediated endocytosis represents a significant route for nanoparticle uptake (Rappoport et al., 2012; Palocci et al., 2017). As depicted in Figure 10B, the fold change of the PCC values (shown in Figure 10A) for all nanobioconjugates slightly decreased at both exposure times compared to values prior to inhibition (Figure 9B). Clathrin-mediated endocytosis is one of the main routes by which internalized nanoparticles end up in endosomes (Doherty and McMahon, 2009; McMahon and Boucrot, 2011; Hu et al., 2015), explaining the observed decrease in PCC percentages. These results are consistent with the previous findings, showing that the LG11-nanobioconjugate still exhibited the highest endosomal escape. The uptake of nanobioconjugates by Vero cells, following clathrin-mediated endocytosis inhibition, revealed also important insights (Figure 10C). The inhibition mainly affected the uptake of the SR11-nanobioconjugate and the MNPs at the 30-min mark, indicating that their initial uptake is largely mediated by clathrin-dependent endocytosis. Over time, these nanoparticles were internalized by alternative routes. Notably, the LG11-nanobioconjugate, with the exposed motif, exhibited the highest area coverage percentages, surpassing 80% at both time points studied. This suggests that the LG11-nanobioconjugate predominantly utilizes alternative endocytic pathways such as macropinocytosis, caveolin-mediated endocytosis, or clathrin/caveolin-independent endocytosis for cellular uptake.

Figure 10D provides a clearer depiction of the percentage of cellular uptake by internalization mechanisms for each nanobioconjugate. This value was estimated from the cell area coverage percentages previously obtained. The results reveal that clathrin-mediated internalization occurs at a higher rate within the first 30 min for almost all nanobioconjugates compared to a longer exposure period of 4 h. Notably, the LG11-nanobioconjugate displays a distinct pattern. It not only has the lowest percentage of uptake via this route but also shows a slight increase from 8.57% at 30 min to 11.1% at 4 h. Despite this lower entry percentage, the LG11-nanobioconjugate demonstrates the highest overall uptake, indicating that it relies more heavily on alternative endocytic pathways for cellular uptake. As previously noted, well-known routes for the transportation of IONPs include caveolin-mediated endocytosis and macropinocytosis (Martín et al., 2011; Neves-Coelho et al., 2017; Salloum et al., 2019; Rueda-Gensini et al., 2020). The uptake of the LG11-nanobioconjugate might be primarily influenced by its surface charge over long-term uptake, as its behavior is similar to that of the anionic bare MNPs. However, the initial low uptake via the clathrin-mediated route is not likely due to its surface charge, as the bare MNPs showed higher uptake. This suggests that the motif influences the activation of other internalization mechanisms. To fully understand the internalization mechanisms of the LG11-nanobioconjugate and the impact of its exposed motif, it is crucial to investigate alternative routes such as caveolin-mediated endocytosis, clathrin- and caveolin-independent endocytosis, and phagocytosis (Doherty and McMahon, 2009; McMahon and Boucrot, 2011; Bohdanowicz and Grinstein, 2013; Qiu et al., 2023). For the SR11 and SG11 nanobioconjugates, where the motif is not exposed, cellular uptake may be mediated by their cationic charge, potentially through energy-independent pathways like direct penetration (Szabó et al., 2021). Moreover, previous studies have demonstrated that cationic MNPs can induce endocytosis via alternative pathways such as micropinocytosis (Pang et al., 2015; Rueda-Gensini et al., 2020; Li and Pang, 2021; Szabó et al., 2021).

Overall, these results have demonstrated that the position of the motif within the peptides significantly affects cellular uptake. The three peptides evaluated, all containing the motif of interest, exhibited varying internalization percentages through the clathrin-mediated pathway. This observation indicates that both the motif itself and its position within the peptide structure influence the internalization mechanisms. For instance, the LG11-nanobioconjugate showed the least internalization through the clathrin-mediated route, suggesting that its exposed motif predominantly influences the peptide's alternative uptake mechanisms.

Conclusion

In this study, we evaluated the effect of the position of the cell-penetrating motif (LFVCR) within peptide-based magnetite nanobioconjugates on biocompatibility, cellular uptake, endosomal escape, and clathrin-mediated endocytosis activation. All peptide sequences displayed the same physicochemical characteristics in terms of size, molecular weight, net charge at pH 7, GRAVY, pI, hydrophobicity, hydrophobic moment, and Boman Index. However, slight differences were observed in the biocompatibility of the designed nanobioconjugates. Notably, the nanobioconjugate with the most exposed motif exhibited higher cellular uptake and enhanced endosomal escape compared to the other designed nanobioconjugates and those with previously reported CPPs. While clathrin-mediated endocytosis is a primary route for nanoparticle uptake, the results showed that the nanobioconjugate with the exposed motif did not primarily enter cells via this pathway, unlike the nanobioconjugates with less exposed motif. This suggests that the position of the motif significantly influences the internalization mechanisms. These results open the opportunity to study other cellular uptake routes involved in the internalization of these IONPs. The final nanobioconjugate displayed suitable characteristics in terms of size, morphology, thermal stability, biocompatibility, cellular uptake, and endosomal escape, making it promising for applications such as diagnostics, magnetic drug and gene delivery, hyperthermia, magnetic resonance imaging, and

theranostics. We hope this research encourages future studies to select immobilization techniques that ensure the correct immobilization of peptides. This study highlights that proper immobilization is crucial for the functionality of the peptides, as inefficient interactions can compromise their efficacy.

Data availability statement

The original contributions presented in the study are included in the article/Supplementary Material, further inquiries can be directed to the corresponding authors.

Ethics statement

The studies involving humans were approved by Ethical Committee at the Universidad de Los Andes, minute number 928–2018. The studies were conducted in accordance with the local legislation and institutional requirements. The participants provided their written informed consent to participate in this study.

Author contributions

LS: Conceptualization, Data curation, Formal Analysis, Investigation, Methodology, Writing–original draft. PC-D: Conceptualization, Data curation, Formal Analysis, Investigation, Methodology, Writing–original draft. JO: Visualization, Writing–review and editing. CM-C: Resources, Supervision, Writing–review and editing. LR: Funding acquisition, Resources, Supervision, Writing–review and editing. VQ: Conceptualization, Formal Analysis, Investigation, Methodology, Writing–original draft, Writing–review and editing. JC: Conceptualization, Funding acquisition, Resources, Supervision, Writing–review and editing.

Funding

The author(s) declare that financial support was received for the research, authorship, and/or publication of this article. This work was funded by the Colombian Ministry of Science, Technology, and Innovation (Minciencias) Grant Contract # 624–2022. Also, we would like to acknowledge the Vice Presidency of Research and Creation's Publication Fund at Universidad de Los Andes.

Acknowledgments

The authors acknowledge the instruments and scientific and technical assistance of the MicroCore Microscopy Core at the Universidad de Los Andes, a facility that is supported by the vicepresidency for research and creation. The authors acknowledge the use of OpenAI's ChatGPT (version GPT-4, model "gpt-4-turbo-16k") to improve the clarity and readability of the manuscript. This tool was employed as part of the writing and editing process.

Conflict of interest

The authors declare that the research was conducted in the absence of any commercial or financial relationships that could be construed as a potential conflict of interest.

The author(s) declared that they were an editorial board member of Frontiers, at the time of submission. This had no impact on the peer review process and the final decision.

Publisher's note

Supplementary material

The Supplementary Material for this article can be found online at: https://www.frontiersin.org/articles/10.3389/fbioe.2024.1450694/full#supplementary-material

References

Ahmad, A., Khan, J. M., and Haque, S. (2019). Strategies in the design of endosomolytic agents for facilitating endosomal escape in nanoparticles. *Biochimie* 160, 61–75. doi:10.1016/j.biochi.2019.02.012

Almaghrabi, M., Alqurshi, A., Jadhav, S., Mazzacuva, F., Cilibrizzi, A., Raimi-Abraham, B., et al. (2023). Evaluating thermogravimetric analysis for the measurement of drug loading in mesoporous silica nanoparticles (MSNs). *Thermochim. Acta* 730, 179616. doi:10.1016/j.tca.2023.179616

Anik, M. I., Hossain, M. K., Hossain, I., Mahfuz, A. M. U. B., Rahman, M. T., and Ahmed, I. (2021). Recent progress of magnetic nanoparticles in biomedical applications: a review. *Nano Sel.* 2 (6), 1146–1186. doi:10.1002/nano.202000162

Appelbaum, J. S., LaRochelle, J., Smith, B., Balkin, D., Holub, J., and Schepartz, A. (2012). Arginine topology controls escape of minimally cationic proteins from early endosomes to the cytoplasm. *Chem. and Biol.* 19 (7), 819–830. doi:10.1016/j.chembiol.2012.05.022

Avsievich, T., Popov, A., Bykov, A., and Meglinski, I. (2019). Mutual interaction of red blood cells influenced by nanoparticles. *Sci. Rep.* 9 (1), 5147. doi:10.1038/s41598-019-41643-x

Barth, A. (2007). Infrared spectroscopy of proteins. *Biochimica Biophysica Acta (BBA) - Bioenergetics* 1767 (9), 1073–1101. doi:10.1016/j.bbabio.2007.06.004

Bhattacharjee, S. (2016). DLS and zeta potential – what they are and what they are not? *J. Control. Release* 235, 337–351. doi:10.1016/j.jconrel.2016.06.017

Bian, Y., Kim, K., Ngo, T., Kim, I., Bae, O. N., Lim, K. M., et al. (2019). Silver nanoparticles promote procoagulant activity of red blood cells: a potential risk of thrombosis in susceptible population. *Part. Fibre Toxicol.* 16 (1), 9. doi:10.1186/s12989-019-0292-6

Biţa, A.-I., Antoniac, I., Miculescu, M., Stan, G. E., Leonat, L., Antoniac, A., et al. (2022). Electrochemical and *in vitro* biological evaluation of bio-active coatings deposited by magnetron sputtering onto biocompatible Mg-0.8Ca alloy. *Materials* 15 (9), 3100. doi:10.3390/ma15093100

Bohdanowicz, M., and Grinstein, S. (2013). Role of phospholipids in endocytosis, phagocytosis, and macropinocytosis. *Physiol. Rev.* 93 (1), 69–106. doi:10.1152/physrev.00002.2012

Bolhassani, A. (2011). Potential efficacy of cell-penetrating peptides for nucleic acid and drug delivery in cancer. *Biochimica Biophysica Acta (BBA) - Rev. Cancer* 1816 (2), 232–246. doi:10.1016/j.bbcan.2011.07.006

Boman, H. G. (2003). Antibacterial peptides: basic facts and emerging concepts. *J. Intern. Med.* 254 (3), 197–215. doi:10.1046/j.1365-2796.2003.01228.x

Chen, D., Monteiro-Riviere, N. A., and Zhang, L. W. (2017). Intracellular imaging of quantum dots, gold, and iron oxide nanoparticles with associated endocytic pathways. *WIREs Nanomedicine Nanobiotechnology* 9 (2). doi:10.1002/wnan.1419

Chen, L., Zhang, Q., Yuan, X., Cao, Y., Yuan, Y., Yin, H., et al. (2017). How charge distribution influences the function of membrane-active peptides: lytic or cell-penetrating? *Int. J. Biochem. and Cell Biol.* 83, 71–75. doi:10.1016/j.biocel.2016.12.011

Chen, Y., Lian, G., Liao, C., Wang, W., Zeng, L., Qian, C., et al. (2013). Characterization of polyethylene glycol-grafted polyethylenimine and superparamagnetic iron oxide nanoparticles (PEG-g-PEI-SPION) as an MRI-visible vector for siRNA delivery in gastric cancer *in vitro* and *in vivo*. *J. Gastroenterology* 48 (7), 809–821. doi:10.1007/s00535-012-0713-x

Chircov, C., Bîrcă, A. C., Dănciulescu, L. A., Neacșu, I. A., Oprea, O. C., Truşcă, R. D., et al. (2023). Usnic acid-loaded magnetite nanoparticles—a comparative study between synthesis methods. *Molecules* 28 (13), 5198. doi:10.3390/molecules28135198

Choi, W., Mahajan, U., Lee, S. M., Abiade, J., and Singh, R. K. (2004). Effect of slurry ionic salts at dielectric silica CMP. *J. Electrochem. Soc.* 151 (3), G185. doi:10.1149/1.1644609

Cifuentes, J., Cifuentes-Almanza, S., Ruiz Puentes, P., Quezada, V., González Barrios, A. F., Calderón-Peláez, M. A., et al. (2023). Multifunctional magnetoliposomes as drug delivery vehicles for the potential treatment of Parkinson's disease. *Front. Bioeng. Biotechnol.* 11, 1181842. doi:10.3389/fbioe.2023.1181842

Console, S., Marty, C., García-Echeverría, C., Schwendener, R., and Ballmer-Hofer, K. (2003). Antennapedia and HIV transactivator of transcription (TAT) "protein transduction domains" promote endocytosis of high molecular weight cargo upon binding to cell surface glycosaminoglycans. *J. Biol. Chem.* 278 (37), 35109–35114. doi:10.1074/jbc.M301726200

Cuellar, M., Cifuentes, J., Perez, J., Suarez-Arnedo, A., Serna, J., Groot, H., et al. (2018). Novel BUF2-magnetite nanobioconjugates with cell-penetrating abilities. *Int. J. Nanomedicine* 13, 8087–8094. doi:10.2147/IJN.S188074

Danaei, M., Dehghankhold, M., Ataei, S., Hasanzadeh Davarani, F., Javanmard, R., Dokhani, A., et al. (2018). Impact of particle size and polydispersity index on the clinical applications of lipidic nanocarrier systems. *Pharmaceutics* 10 (2), 57. doi:10.3390/pharmaceutics10020057

De Meutter, J., and Goormaghtigh, E. (2021). Evaluation of protein secondary structure from FTIR spectra improved after partial deuteration. *Eur. Biophysics J.* 50 (3–4), 613–628. doi:10.1007/s00249-021-01502-y

Deng, H., Li, X., Peng, Q., Wang, X., Chen, J., and Li, Y. (2005). Monodisperse magnetic single-crystal ferrite microspheres. *Angew. Chem. Int. Ed.* 44 (18), 2782–2785. doi:10.1002/anie.200462551

Derakhshankhah, H., and Jafari, S. (2018). Cell penetrating peptides: a concise review with emphasis on biomedical applications. *Biomed. and Pharmacother.* 108, 1090–1096. doi:10.1016/j.biopha.2018.09.097

Derossi, D., Calvet, S., Trembleau, A., Brunissen, A., Chassaing, G., and Prochiantz, A. (1996). Cell internalization of the third helix of the antennapedia homeodomain is receptor-independent. *J. Biol. Chem.* 271 (30), 18188–18193. doi:10.1074/jbc.271.30.18188

Doherty, G. J., and McMahon, H. T. (2009). Mechanisms of endocytosis. *Annu. Rev. Biochem.* 78 (1), 857–902. doi:10.1146/annurev.biochem.78.081307.110540

Eckel, R., Huo, H., Guan, H. W., Hu, X., Che, X., and Huang, W. D. (2001). Characteristic infrared spectroscopic patterns in the protein bands of human breast cancer tissue. *Vib. Spectrosc.* 27 (2), 165–173. doi:10.1016/S0924-2031(01)00134-5

El-Andaloussi, S., Holm, T., and Langel, U. (2005). Cell-penetrating peptides: mechanisms and applications. *Curr. Pharm. Des.* 11 (28), 3597–3611. doi:10.2174/138161205774580796

Erazo-Oliveras, A., Muthukrishnan, N., Baker, R., Wang, T. Y., and Pellois, J. P. (2012). Improving the endosomal escape of cell-penetrating peptides and their cargos: strategies and challenges. *Pharmaceuticals* 5 (11), 1177–1209. doi:10.3390/ph5111177

Fadnavis, N. W., Bhaskar, V., Kantam, M. L., and Choudary, B. M. (2003). Highly efficient "tight fit" immobilization of α-chymotrypsin in mesoporous MCM-41: a novel approach using precursor immobilization and activation. *Biotechnol. Prog.* 19 (2), 346–351. doi:10.1021/bp025678s

Farkhani, S. M., Valizadeh, A., Karami, H., Mohammadi, S., Sohrabi, N., and Badrzadeh, F. (2014). Cell penetrating peptides: efficient vectors for delivery of nanoparticles, nanocarriers, therapeutic and diagnostic molecules. *Peptides* 57, 78–94. doi:10.1016/j.peptides.2014.04.015

Fatima, H., Charinpanitkul, T., and Kim, K.-S. (2021). Fundamentals to apply magnetic nanoparticles for hyperthermia therapy. *Nanomaterials* 11 (5), 1203. doi:10.3390/nano11051203

Ferreira, L. P., Reis, C. P., Robalo, T. T., Melo Jorge, M. E., Ferreira, P., Gonçalves, J., et al. (2022). Assisted synthesis of coated iron oxide nanoparticles for magnetic hyperthermia. *Nanomaterials* 12 (11), 1870. doi:10.3390/nano12111870

Fischer, R., Waizenegger, T., Köhler, K., and Brock, R. (2002). A quantitative validation of fluorophore-labelled cell-permeable peptide conjugates: fluorophore and cargo dependence of import. *Biochimica Biophysica Acta (BBA) - Biomembr.* 1564 (2), 365–374. doi:10.1016/S0005-2736(02)00471-6

Fittipaldi, A., Ferrari, A., Zoppé, M., Arcangeli, C., Pellegrini, V., Beltram, F., et al. (2003). Cell membrane lipid rafts mediate caveolar endocytosis of HIV-1 tat fusion proteins. *J. Biol. Chem.* 278 (36), 34141–34149. doi:10.1074/jbc.M303045200

Fleming, E., Maharaj, N. P., Chen, J. L., Nelson, R. B., and Elmore, D. E. (2008). Effect of lipid composition on buforin II structure and membrane entry. *Proteins Struct. Funct. Bioinforma.* 73 (2), 480–491. doi:10.1002/prot.22074

Fologea, D., Ledden, B., McNabb, D. S., and Li, J. (2007). Electrical characterization of protein molecules by a solid-state nanopore. *Appl. Phys. Lett.* 91 (5), 539011–539013. doi:10.1063/1.2767206

Fröhlich, E. (2012). The role of surface charge in cellular uptake and cytotoxicity of medical nanoparticles. *Int. J. Nanomedicine* 7, 5577–5591. doi:10.2147/IJN.S36111

Gambaryan, S., and Tsikas, D. (2015). A review and discussion of platelet nitric oxide and nitric oxide synthase: do blood platelets produce nitric oxide from l-arginine or nitrite? *Amino Acids* 47 (9), 1779–1793. doi:10.1007/s00726-015-1986-1

Gawrys, J., Gajecki, D., Szahidewicz-Krupska, E., and Doroszko, A. (2020). Intraplatelet L-arginine-nitric oxide metabolic pathway: from discovery to clinical implications in prevention and treatment of cardiovascular disorders. *Oxidative Med. Cell. Longev.* 2020, 1–11. doi:10.1155/2020/1015908

Gessner, I., and Neundorf, I. (2020). Nanoparticles modified with cell-penetrating peptides: conjugation mechanisms, physicochemical properties, and application in cancer diagnosis and therapy. *Int. J. Mol. Sci.* 21 (7), 2536. doi:10.3390/ijms21072536

Gomez, J. A., Chen, J., Ngo, J., Hajkova, D., Yeh, I. J., Gama, V., et al. (2010). Cell-penetrating penta-peptides (CPP5s): measurement of cell entry and protein-transduction activity. *Pharmaceuticals* 3 (12), 3594–3613. doi:10.3390/ph3123594

Green, M., and Loewenstein, P. M. (1988). Autonomous functional domains of chemically synthesized human immunodeficiency virus tat trans-activator protein. *Cell* 55 (6), 1179–1188. doi:10.1016/0092-8674(88)90262-0

Grigorieva, M. E., Obergan, T.Y., and Lyapina, L. A. (2023). Anticoagulation effects of leucine-containing glyprolines in hypercoagulation. *Biol. Bull.* 50 (6), 1351–1355. doi:10.1134/S1062359023603300

Hällbrink, M., Florén, A., Elmquist, A., Pooga, M., Bartfai, T., and Langel, Ü. (2001). Cargo delivery kinetics of cell-penetrating peptides. *Biochimica Biophysica Acta (BBA) - Biomembr.* 1515 (2), 101–109. doi:10.1016/S0005-2736(01)00398-4

Harjo, M., Torop, J., Järvekülg, M., Tamm, T., and Kiefer, R. (2019). Electrochemomechanical behavior of polypyrrole-coated nanofiber scaffolds in cell culture medium. *Polymers* 11 (6), 1043. doi:10.3390/polym11061043

Harush-Frenkel, O., Debotton, N., Benita, S., and Altschuler, Y. (2007). Targeting of nanoparticles to the clathrin-mediated endocytic pathway. *Biochem. Biophysical Res. Commun.* 353 (1), 26–32. doi:10.1016/j.bbrc.2006.11.135

Henao, M. C., Ocasion, C., Puentes, P. R., González-Melo, C., Quezada, V., Cifuentes, J., et al. (2022). Translocating peptides of biomedical interest obtained from the spike (S) glycoprotein of the SARS-CoV-2. *Membranes* 12 (6), 600. doi:10.3390/membranes12060600

Hersh, A. M., Alomari, S., and Tyler, B. M. (2022). Crossing the blood-brain barrier: advances in nanoparticle Technology for drug delivery in neuro-oncology. *Int. J. Mol. Sci.* 23 (8), 4153. doi:10.3390/ijms23084153

Hondow, N., Brydson, R., Wang, P., Holton, M. D., Brown, M. R., Rees, P., et al. (2012). Quantitative characterization of nanoparticle agglomeration within biological media. *J. Nanoparticle Res.* 14 (7), 977. doi:10.1007/s11051-012-0977-3

Hu, Y.-B., Dammer, E. B., Ren, R. J., and Wang, G. (2015). The endosomal-lysosomal system: from acidification and cargo sorting to neurodegeneration. *Transl. Neurodegener.* 4 (1), 18. doi:10.1186/s40035-015-0041-1

Hynes, R. O. (2002). Integrins. *Cell* 110 (6), 673–687. doi:10.1016/S0092-8674(02)00971-6

International Organization for Standardization (2018). *ISO 10993- 4:2017 Biological evaluation of medical devices. Part 4: selection of tests for interactions with blood.* Geneva: ISO.

ISO (2009). *ISO 10993- 5:2009 Biological evaluation of medical devices. Part 5: tests for* in vitro *cytotoxicity*. Geneva: ISO.

Jackson, M., and Mantsch, H. H. (1995). The use and misuse of FTIR spectroscopy in the determination of protein structure. *Crit. Rev. Biochem. Mol. Biol.* 30 (2), 95–120. doi:10.3109/10409239509085140

Järver, P., and Langel, Ü. (2006). Cell-penetrating peptides—a brief introduction. *Biochimica Biophysica Acta (BBA) - Biomembr.* 1758 (3), 260–263. doi:10.1016/j.bbamem.2006.02.012

Ji, Z., Jin, X., George, S., Xia, T., Meng, H., Wang, X., et al. (2010). Dispersion and stability optimization of TiO2 nanoparticles in cell culture media. *Environ. Sci. and Technol.* 44 (19), 7309–7314. doi:10.1021/es100417s

Kaewsichan, L., Riyapan, D., Prommajan, P., and Kaewsrichan, J. (2011). Effects of sintering temperatures on micro-morphology, mechanical properties, and bioactivity of

bone scaffolds containing calcium silicate. *ScienceAsia* 37 (3), 240. doi:10.2306/scienceasia1513-1874.2011.37.240

Karlsson, J., Ungell, A. L., Gråsjö, J., and Artursson, P. (1999). Paracellular drug transport across intestinal epithelia: influence of charge and induced water flux. *Eur. J. Pharm. Sci.* 9 (1), 47–56. doi:10.1016/S0928-0987(99)00041-X

Kobayashi, T., Startchev, K., Whitney, A. J., and Gruenberg, J. (2001). Localization of lysobisphosphatidic acid-rich membrane domains in late endosomes. *Biol. Chem.* 382 (3), 483–485. doi:10.1515/BC.2001.059

Kong, J., and Yu, S. (2007). Fourier transform infrared spectroscopic analysis of protein secondary structures. *Acta Biochimica Biophysica Sinica* 39 (8), 549–559. doi:10.1111/j.1745-7270.2007.00320.x

Koren, E., and Torchilin, V. P. (2012). Cell-penetrating peptides: breaking through to the other side. *Trends Mol. Med.* 18 (7), 385–393. doi:10.1016/j.molmed.2012.04.012

Krispin, M., Ullrich, A., and Horn, S. (2012). Crystal structure of iron-oxide nanoparticles synthesized from ferritin. *J. Nanoparticle Res.* 14 (2), 669. doi:10.1007/s11051-011-0669-4

Kudr, J., Haddad, Y., Richtera, L., Heger, Z., Cernak, M., Adam, V., et al. (2017). Magnetic nanoparticles: from design and synthesis to real world applications. *Nanomaterials* 7 (9), 243. doi:10.3390/nano7090243

Kumosinski, T. F., and Farrell, H. M. (1993). Determination of the global secondary structure of proteins by Fourier transform infrared (FTIR) spectroscopy. *Trends Food Sci. and Technol.* 4 (6), 169–175. doi:10.1016/0924-2244(93)90119-U

Kyte, J., and Doolittle, R. F. (1982). A simple method for displaying the hydropathic character of a protein. *J. Mol. Biol.* 157 (1), 105–132. doi:10.1016/0022-2836(82)90515-0

Lahiri, B. B., Ranoo, S., Zaibudeen, A., and Philip, J. (2017). Magnetic hyperthermia in magnetic nanoemulsions: effects of polydispersity, particle concentration and medium viscosity. *J. Magnetism Magnetic Mater.* 441, 310–327. doi:10.1016/j.jmmm.2017.05.076

Lamiable, A., Thévenet, P., Rey, J., Vavrusa, M., Derreumaux, P., and Tufféry, P. (2016). PEP-FOLD3: faster *de novo* structure prediction for linear peptides in solution and in complex. *Nucleic Acids Res.* 44 (W1), W449–W454. doi:10.1093/nar/gkw329

Lee, M.-T., Hung, W. C., Chen, F. Y., and Huang, H. W. (2005). Many-body effect of antimicrobial peptides: on the correlation between lipid's spontaneous curvature and pore formation. *Biophysical J.* 89 (6), 4006–4016. doi:10.1529/biophysj.105.068080

Lewis, S. P., Lewis, A. T., and Lewis, P. D. (2013). Prediction of glycoprotein secondary structure using ATR-FTIR. *Vib. Spectrosc.* 69, 21–29. doi:10.1016/j.vibspec.2013.09.001

Li, L., Li, D., and Zhang, Z. (2022). Colloidal stability of magnetite nanoparticles coated by oleic acid and 3-(N,N-Dimethylmyristylammonio)propanesulfonate in solvents. *Front. Mater.* 9. doi:10.3389/fmats.2022.893072

Li, Y.-X., and Pang, H.-B. (2021). Macropinocytosis as a cell entry route for peptide-functionalized and bystander nanoparticles. *J. Control. Release* 329, 1222–1230. doi:10.1016/j.jconrel.2020.10.049

Liang, W., and Lam, J. K. (2012). "Endosomal escape pathways for non-viral nucleic acid delivery systems," in *Molecular regulation of endocytosis* (London: InTech). doi:10.5772/46006

Loganathan, S., Valapa, R. B., Mishra, R. K., Pugazhenthi, G., and Thomas, S. (2017). "Thermogravimetric analysis for characterization of nanomaterials," in *Thermal and rheological measurement techniques for nanomaterials characterization* (Elsevier), 67–108.

Lopez-Barbosa, N., Garcia, J. G., Cifuentes, J., Castro, L. M., Vargas, F., Ostos, C., et al. (2020). Multifunctional magnetite nanoparticles to enable delivery of siRNA for the potential treatment of Alzheimer's. *Drug Deliv.* 27 (1), 864–875. doi:10.1080/10717544.2020.1775724

Lundberg, P., and Langel, Ü. (2003). A brief introduction to cell-penetrating peptides. *J. Mol. Recognit.* 16 (5), 227–233. doi:10.1002/jmr.630

Lunov, O., Zablotskii, V., Syrovets, T., Röcker, C., Tron, K., Nienhaus, G. U., et al. (2011). Modeling receptor-mediated endocytosis of polymer-functionalized iron oxide nanoparticles by human macrophages. *Biomaterials* 32 (2), 547–555. doi:10.1016/j.biomaterials.2010.08.111

Luther, E. M., Petters, C., Bulcke, F., Kaltz, A., Thiel, K., Bickmeyer, U., et al. (2013). Endocytotic uptake of iron oxide nanoparticles by cultured brain microglial cells. *Acta Biomater.* 9 (9), 8454–8465. doi:10.1016/j.actbio.2013.05.022

Macia, E., Ehrlich, M., Massol, R., Boucrot, E., Brunner, C., and Kirchhausen, T. (2006). Dynasore, a cell-permeable inhibitor of dynamin. *Dev. Cell* 10 (6), 839–850. doi:10.1016/j.devcel.2006.04.002

Madani, F., Lindberg, S., Langel, Ü., Futaki, S., and Gräslund, A. (2011). Mechanisms of cellular uptake of cell-penetrating peptides. *J. Biophysics* 2011, 1–10. doi:10.1155/2011/414729

Martín, I., Teixidó, M., and Giralt, E. (2011). Design, synthesis and characterization of a New anionic cell-penetrating peptide: SAP(E). *ChemBioChem* 12 (6), 896–903. doi:10.1002/cbic.201000679

Matsumoto, R., Okochi, M., Shimizu, K., Kanie, K., Kato, R., and Honda, H. (2015). Effects of the properties of short peptides conjugated with cell-penetrating peptides on their internalization into cells. *Sci. Rep.* 5 (1), 12884. doi:10.1038/srep12884

Matsuo, H., Chevallier, J., Mayran, N., Le Blanc, I., Ferguson, C., Faure´, J., et al. (2004). Role of LBPA and alix in multivesicular liposome formation and endosome organization. *Science* 303 (5657), 531–534. doi:10.1126/science.1092425

Matsuzaki, K., Yoneyama, S., Murase, O., and Miyajima, K. (1996). Transbilayer transport of ions and lipids coupled with mastoparan X translocation. *Biochemistry* 35 (25), 8450–8456. doi:10.1021/bi960342a

Mayor, S., and Pagano, R. E. (2007). Pathways of clathrin-independent endocytosis. *Nat. Rev. Mol. Cell Biol.* 8 (8), 603–612. doi:10.1038/nrm2216

Mbeh, D. A., Javanbakht, T., Tabet, L., Merhi, Y., Maghni, K., Sacher, E., et al. (2015). Protein corona formation on magnetite nanoparticles: effects of culture medium composition, and its consequences on superparamagnetic nanoparticle cytotoxicity. *J. Biomed. Nanotechnol.* 11 (5), 828–840. doi:10.1166/jbn.2015.2000

McCluskey, A., Daniel, J. A., Hadzic, G., Chau, N., Clayton, E. L., Mariana, A., et al. (2013). Building a better Dynasore: the dyngo compounds potently inhibit dynamin and endocytosis. *Traffic* 14 (12), 1272–1289. doi:10.1111/tra.12119

McDaniel, J. K., Abdelgawwad, M. S., Hargett, A., Renfrow, M. B., Bdeir, K., Cao, W., et al. (2019). Human neutrophil peptide-1 inhibits thrombus formation under arterial flow via its terminal free cysteine thiols. *J. Thrombosis Haemostasis* 17 (4), 596–606. doi:10.1111/jth.14407

McMahon, H. T., and Boucrot, E. (2011). Molecular mechanism and physiological functions of clathrin-mediated endocytosis. *Nat. Rev. Mol. Cell Biol.* 12 (8), 517–533. doi:10.1038/nrm3151

Montiel Schneider, M. G., Martín, M. J., Otarola, J., Vakarelska, E., Simeonov, V., Lassalle, V., et al. (2022). Biomedical applications of iron oxide nanoparticles: current insights progress and perspectives. *Pharmaceutics* 14 (1), 204. doi:10.3390/pharmaceutics14010204

Neundorf, I. (2019). Antimicrobial and cell-penetrating peptides: how to understand two distinct functions despite similar physicochemical properties. *Adv. Exp. Med. Biol.* 1117, 93–109. doi:10.1007/978-981-13-3588-4_7

Neves-Coelho, S., Eleutério, R., Enguita, F., Neves, V., and Castanho, M. (2017). A New noncanonical anionic peptide that translocates a cellular blood–brain barrier model. *Molecules* 22 (10), 1753. doi:10.3390/molecules22101753

Nguyen, M. D., Tran, H. V., Xu, S., and Lee, T. R. (2021). Fe3O4 nanoparticles: structures, synthesis, magnetic properties, surface functionalization, and emerging applications. *Appl. Sci.* 11 (23), 11301. doi:10.3390/app112311301

Nica, V., Marino, A., Pucci, C., Şen, Ö., Emanet, M., De Pasquale, D., et al. (2023). Cell-membrane-coated and cell-penetrating peptide-conjugated trimagnetic nanoparticles for targeted magnetic hyperthermia of prostate cancer cells. *ACS Appl. Mater. and Interfaces* 15 (25), 30008–30028. doi:10.1021/acsami.3c07248

Ortega, G., and Reguera, E. (2019). "Biomedical applications of magnetite nanoparticles," in *Materials for biomedical engineering* (Elsevier), 397–434.

Orts-Gil, G., Natte, K., Drescher, D., Bresch, H., Mantion, A., Kneipp, J., et al. (2011). Characterisation of silica nanoparticles prior to *in vitro* studies: from primary particles to agglomerates. *J. Nanoparticle Res.* 13 (4), 1593–1604. doi:10.1007/s11051-010-9910-9

Palocci, C., Valletta, A., Chronopoulou, L., Donati, L., Bramosanti, M., Brasili, E., et al. (2017). Endocytic pathways involved in PLGA nanoparticle uptake by grapevine cells and role of cell wall and membrane in size selection. *Plant Cell Rep.* 36 (12), 1917–1928. doi:10.1007/s00299-017-2206-0

Pang, H.-B., Braun, G. B., and Ruoslahti, E. (2015). Neuropilin-1 and heparan sulfate proteoglycans cooperate in cellular uptake of nanoparticles functionalized by cationic cell-penetrating peptides. *Sci. Adv.* 1 (10), e1500821. doi:10.1126/sciadv.1500821

Park, C. B., Kim, M. S., and Kim, S. C. (1996). A novel antimicrobial peptide fromBufo bufo gargarizans. *Biochem. Biophysical Res. Commun.* 218 (1), 408–413. doi:10.1006/bbrc.1996.0071

Park, C. B., Yi, K. S., Matsuzaki, K., Kim, M. S., and Kim, S. C. (2000). Structure–activity analysis of buforin II, a histone H2A-derived antimicrobial peptide: the proline hinge is responsible for the cell-penetrating ability of buforin II. *Proc. Natl. Acad. Sci.* 97 (15), 8245–8250. doi:10.1073/pnas.150518097

Perez, J., Rueda, J., Cuellar, M., Suarez-Arnedo, A., Cruz, J. C., and Muñoz-Camargo, C. (2019). Cell-penetrating and antibacterial BUF-II nanobioconjugates: enhanced potency via immobilization on polyetheramine-modified magnetite nanoparticles. *Int. J. Nanomedicine* 14, 8483–8497. doi:10.2147/IJN.S224286

Petrov, K., and Chubarov, A. (2022). Magnetite nanoparticles for biomedical applications. *Encyclopedia* 2 (4), 1811–1828. doi:10.3390/encyclopedia2040125

Piccini, L. E., Castilla, V., and Damonte, E. B. (2015). Dengue-3 virus entry into Vero cells: role of clathrin-mediated endocytosis in the outcome of infection. *PLOS ONE* 10 (10), e0140824. doi:10.1371/journal.pone.0140824

Portilla, Y., Mulens-Arias, V., Daviu, N., Paradela, A., Pérez-Yagüe, S., and Barber, D. F. (2023). Interaction of iron oxide nanoparticles with macrophages is influenced distinctly by "self" and "non-self" biological identities. *ACS Appl. Mater. and Interfaces* 15 (30), 35906–35926. doi:10.1021/acsami.3c05555

Pouny, Y., Rapaport, D., Mor, A., Nicolas, P., and Shai, Y. (1992). Interaction of antimicrobial dermaseptin and its fluorescently labeled analogs with phospholipid membranes. *Biochemistry* 31 (49), 12416–12423. doi:10.1021/bi00164a017

Preta, G., Cronin, J. G., and Sheldon, I. M. (2015). Dynasore - not just a dynamin inhibitor. *Cell Commun. Signal.* 13 (1), 24. doi:10.1186/s12964-015-0102-1

Qin, T., Huang, X., Zhang, Q., Chen, F., Zhu, J., and Ding, Y. (2023). Hemostatic effects of FmocF-ADP hydrogel consisted of Fmoc-Phenylalanine and ADP. *Amino Acids* 55 (4), 499–507. doi:10.1007/s00726-023-03243-y

Qiu, C., Xia, F., Zhang, J., Shi, Q., Meng, Y., Wang, C., et al. (2023). Advanced strategies for overcoming endosomal/lysosomal barrier in nanodrug delivery. *Research* 6, 0148. doi:10.34133/research.0148

Ramírez-Acosta, C. M., Cifuentes, J., Castellanos, M. C., Moreno, R. J., Muñoz-Camargo, C., Cruz, J. C., et al. (2020). PH-responsive, cell-penetrating, core/shell magnetite/silver nanoparticles for the delivery of plasmids: preparation, characterization, and preliminary *in vitro* evaluation. *Pharmaceutics* 12 (6), 561. doi:10.3390/pharmaceutics12060561

Rampling, M. W. (1999). "Rouleaux Formation; its causes and consequences," in *Cardiovascular flow modelling and measurement with application to clinical medicine* (Oxford University PressOxford), 183–193.

Ran, Q., Xiang, Y., Liu, Y., Xiang, L., Li, F., Deng, X., et al. (2015). Eryptosis indices as a novel predictive parameter for biocompatibility of Fe3O4 magnetic nanoparticles on erythrocytes. *Sci. Rep.* 5 (1), 16209. doi:10.1038/srep16209

Rangel-Muñoz, N., Suarez-Arnedo, A., Anguita, R., Prats-Ejarque, G., Osma, J. F., Muñoz-Camargo, C., et al. (2020). Magnetite nanoparticles functionalized with RNases against intracellular infection of *Pseudomonas aeruginosa*. *Pharmaceutics* 12 (7), 631. doi:10.3390/pharmaceutics12070631

Rappoport, J., Smith, P. J., Giroud, M., Wiggins, H. L., Mazzolin, J., and Dyson, J. R. (2012). Cellular entry of nanoparticles via serum sensitive clathrin-mediated endocytosis, and plasma membrane permeabilization. *Int. J. Nanomedicine* 7, 2045–2055. doi:10.2147/IJN.S29334

Richard, J. P., Melikov, K., Vives, E., Ramos, C., Verbeure, B., Gait, M. J., et al. (2003). Cell-penetrating peptides. *J. Biol. Chem.* 278 (1), 585–590. doi:10.1074/jbc.M209548200

Rocha-Santos, T. A. P. (2014). Sensors and biosensors based on magnetic nanoparticles. *TrAC Trends Anal. Chem.* 62, 28–36. doi:10.1016/j.trac.2014.06.016

Rong, L., Qin, S. Y., Zhang, C., Cheng, Y. J., Feng, J., Wang, S. B., et al. (2018). Biomedical applications of functional peptides in nano-systems. *Mater. Today Chem.* 9, 91–102. doi:10.1016/j.mtchem.2018.06.001

Rueda-Gensini, L., Cifuentes, J., Castellanos, M. C., Puentes, P. R., Serna, J. A., Muñoz-Camargo, C., et al. (2020). Tailoring iron oxide nanoparticles for efficient cellular internalization and endosomal escape. *Nanomaterials* 10 (9), 1816. doi:10.3390/nano10091816

Ruiz Puentes, P., Henao, M. C., Cifuentes, J., Muñoz-Camargo, C., Reyes, L. H., Cruz, J. C., et al. (2022). Rational discovery of antimicrobial peptides by means of artificial intelligence. *Membranes* 12 (7), 708. doi:10.3390/membranes12070708

Ruseska, I., and Zimmer, A. (2020). Internalization mechanisms of cell-penetrating peptides. *Beilstein J. Nanotechnol.* 11, 101–123. doi:10.3762/bjnano.11.10

Sadeghi, F., Kajbaf, M., and Shafiee, F. (2022). BR2, a buforin derived cancer specific cell penetrating peptide for targeted delivering of toxic agents: a review article. *Int. J. Peptide Res. Ther.* 28 (3), 93. doi:10.1007/s10989-022-10384-3

Salloum, G., Jakubik, C. T., Erami, Z., Heitz, S. D., Bresnick, A. R., and Backer, J. M. (2019). PI3Kβ is selectively required for growth factor-stimulated macropinocytosis. *J. Cell Sci.* 132 (16), jcs231639. doi:10.1242/jcs.231639

Seifi, H., Gholami, T., Seifi, S., Ghoreishi, S. M., and Salavati-Niasari, M. (2020). A review on current trends in thermal analysis and hyphenated techniques in the investigation of physical, mechanical and chemical properties of nanomaterials. *J. Anal. Appl. Pyrolysis* 149, 104840. doi:10.1016/j.jaap.2020.104840

Serbian, I., Hoenke, S., Kraft, O., and Csuk, R. (2020). Ester and amide derivatives of rhodamine B exert cytotoxic effects on different human tumor cell lines. *Med. Chem. Res.* 29 (9), 1655–1661. doi:10.1007/s00044-020-02591-8

Shariatinia, Z. (2021). "Cell penetration peptide-based nanomaterials in drug delivery and biomedical applications," in *Biopolymer-based nanomaterials in drug delivery and biomedical applications* (Elsevier), 535–588.

Sharma, G., Lakkadwala, S., Modgil, A., and Singh, J. (2016). The role of cell-penetrating peptide and transferrin on enhanced delivery of drug to brain. *Int. J. Mol. Sci.* 17 (6), 806. doi:10.3390/ijms17060806

Shen, Y., Maupetit, J., Derreumaux, P., and Tufféry, P. (2014). Improved PEP-FOLD approach for peptide and miniprotein structure prediction. *J. Chem. Theory Comput.* 10 (10), 4745–4758. doi:10.1021/ct500592m

Shi, J., Zhao, D., Li, X., Ding, F., Tang, X., Liu, N., et al. (2020). The conjugation of rhodamine B enables carrier-free mitochondrial delivery of functional proteins. *Org. and Biomol. Chem.* 18 (35), 6829–6839. doi:10.1039/D0OB01305F

Silhol, M., Tyagi, M., Giacca, M., Lebleu, B., and Vivès, E. (2002). Different mechanisms for cellular internalization of the HIV-1 Tat-derived cell penetrating peptide and recombinant proteins fused to Tat. *Eur. J. Biochem.* 269 (2), 494–501. doi:10.1046/j.0014-2956.2001.02671.x

Silva, S., Almeida, A., and Vale, N. (2019). Combination of cell-penetrating peptides with nanoparticles for therapeutic application: a review. *Biomolecules* 9 (1), 22. doi:10.3390/biom9010022

Sousa de Almeida, M., Susnik, E., Drasler, B., Taladriz-Blanco, P., Petri-Fink, A., and Rothen-Rutishauser, B. (2021). Understanding nanoparticle endocytosis to improve targeting strategies in nanomedicine. *Chem. Soc. Rev.* 50 (9), 5397–5434. doi:10.1039/D0CS01127D

Spicer, C. D., Jumeaux, C., Gupta, B., and Stevens, M. M. (2018). Peptide and protein nanoparticle conjugates: versatile platforms for biomedical applications. *Chem. Soc. Rev.* 47 (10), 3574–3620. doi:10.1039/C7CS00877E

Szabó, I., Illien, F., Dókus, L. E., Yousef, M., Baranyai, Z., Bősze, S., et al. (2021). Influence of the Dabcyl group on the cellular uptake of cationic peptides: short oligoarginines as efficient cell-penetrating peptides. *Amino Acids* 53 (7), 1033–1049. doi:10.1007/s00726-021-03003-w

Thevenet, P., Shen, Y., Maupetit, J., Guyon, F., Derreumaux, P., and Tuffery, P. (2012). PEP-FOLD: an updated *de novo* structure prediction server for both linear and disulfide bonded cyclic peptides. *Nucleic Acids Res.* 40 (W1), W288–W293. doi:10.1093/nar/gks419

Trabulo, S., Cardoso, A. L., Mano, M., and De Lima, M. C. P. (2010). Cell-penetrating peptides—mechanisms of cellular uptake and generation of delivery systems. *Pharmaceuticals* 3 (4), 961–993. doi:10.3390/ph3040961

Wei, G., Wang, Y., Huang, X., Hou, H., and Zhou, S. (2018). Peptide-based nanocarriers for cancer therapy. *Small Methods* 2 (9). doi:10.1002/smtd.201700358

Wiogo, H. T. R., Lim, M., Bulmus, V., Yun, J., and Amal, R. (2011). Stabilization of magnetic iron oxide nanoparticles in biological media by fetal bovine serum (FBS). *Langmuir* 27 (2), 843–850. doi:10.1021/la104278m

Xie, J., Bi, Y., Zhang, H., Dong, S., Teng, L., Lee, R. J., et al. (2020). Cell-penetrating peptides in diagnosis and treatment of human diseases: from preclinical research to clinical application. *Front. Pharmacol.* 11, 697. doi:10.3389/fphar.2020.00697

Xu, Y., Jiang, H., Li, L., Chen, F., Liu, Y., Zhou, M., et al. (2020). Branched-chain amino acid catabolism promotes thrombosis risk by enhancing tropomodulin-3 propionylation in platelets. *Circulation* 142 (1), 49–64. doi:10.1161/CIRCULATIONAHA.119.043581

Yetisgin, A. A., Cetinel, S., Zuvin, M., Kosar, A., and Kutlu, O. (2020). Therapeutic nanoparticles and their targeted delivery applications. *Molecules* 25 (9), 2193. doi:10.3390/molecules25092193

Yu, S.-M., Laromaine, A., and Roig, A. (2014). Enhanced stability of superparamagnetic iron oxide nanoparticles in biological media using a pH adjusted-BSA adsorption protocol. *J. Nanoparticle Res.* 16 (7), 2484. doi:10.1007/s11051-014-2484-1

Yusuf, A., Almotairy, A. R. Z., Henidi, H., Alshehri, O. Y., and Aldughaim, M. S. (2023). Nanoparticles as drug delivery systems: a review of the implication of nanoparticles' physicochemical properties on responses in biological systems. *Polymers* 15 (7), 1596. doi:10.3390/polym15071596

Zavisova, V., Koneracka, M., Gabelova, A., Svitkova, B., Ursinyova, M., Kubovcikova, M., et al. (2019). Effect of magnetic nanoparticles coating on cell proliferation and uptake. *J. Magnetism Magnetic Mater.* 472, 66–73. doi:10.1016/j.jmmm.2018.09.116

Zeng, H., Li, J., Hou, K., Wu, Y., Chen, H., and Ning, Z. (2022). Melanoma and nanotechnology-based treatment. *Front. Oncol.* 12, 858185. doi:10.3389/fonc.2022.858185

Zhao, F., Zhao, Y., Liu, Y., Chang, X., Chen, C., and Zhao, Y. (2011). Cellular uptake, intracellular trafficking, and cytotoxicity of nanomaterials. *Small* 7 (10), 1322–1337. doi:10.1002/smll.201100001

Zhao, J., and Stenzel, M. H. (2018). Entry of nanoparticles into cells: the importance of nanoparticle properties. *Polym. Chem.* 9 (3), 259–272. doi:10.1039/C7PY01603D

Zhu, Y., Yang, Q., Lu, T., Qi, W., Zhang, H., Wang, M., et al. (2020). Effect of phosphate on the adsorption of antibiotics onto iron oxide minerals: comparison between tetracycline and ciprofloxacin. *Ecotoxicol. Environ. Saf.* 205, 111345. doi:10.1016/j.ecoenv.2020.111345